Development of multiscale porous elastomer substrates with passive-cooling capabilities and strain-insensitive conductive nanocomposites for skin-interfaced electronics

---

A Thesis

presented to

the Faculty of the Graduate School

at the University of Missouri-Columbia

In Partial Fulfillment

of the Requirements for the Degree

Master of Science

---

by

QIHUI FEI

Dr. Zheng Yan, Thesis Supervisor

July 2021

The undersigned, appointed by the dean of the Graduate School, have examined the thesis entitled

Development of multiscale porous elastomer substrates with passive-cooling capabilities and strain-insensitive conductive nanocomposites for skin-interfaced electronics

presented by Qihui Fei,

a candidate for the degree of Master of Science,

and hereby certify that, in their opinion, it is worthy of acceptance.

Dr. Zheng Yan, Chemical Engineering

Dr. Qingsong Yu, Mechanical & Aerospace Engineering

Dr. Ilker Ozden, Biomedical, Biological & Chemical Engineering

DEDICATION

I would like to dedicate my work to my family and friends for their support and encouragement. It is especially dedicated to my parents, Jianxin Fei and Xia Feng, for their unconditional love.

ACKNOWLEDGEMENTS

I would like to express my gratitude to those who supported me throughout my life and during the time of my graduate study.

First, I sincerely thank my research advisor, Dr. Zheng Yan, for his encouragement, patient guidance, and useful advice on research work.

My sincere thanks also go to Dr. Qingsong Yu and Dr. Ilker Ozden for their useful suggestions on my thesis. And I appreciate the time and efforts they put in serving on my committee.

I would like to thank my current and former lab mates for all their help on my research : Yadong Xu, Bohan Sun, Yun Ling, Zanyu Chen and Ganggang Zhao. I give my special thanks to Yadong Xu who I worked with on this project for all his help and inspiration.

Finally, I thank my family because I know they will always be with me and give me power.

TABLE OF CONTENTS

LIST OF FIGURES

LIST OF TABLES

ABSTRACT

Emerging skin-interfaced electronics have been playing a significant role in many areas such as clinical healthcare and mobile fitness tracking because they can collect a variety of biological signals from human body. However, conventional electronic materials are usually rigid and brittle, which leads to mechanical mismatch with soft human skin. To overcome the disadvantages, we paid attention to intrinsically stretchable polymer materials.

This work focuses on the synthesis of novel multifunctional porous materials for breathable and intrinsically stretchable skin-interfaced electronics with minimal inflammation risks, outstanding mechanical pliability, and other desired features.

We first report on the fabrication of multiscale porous elastomer supporting substrates with passive cooling properties which means the on-skin electronics made with the porous elastomer substrates can passively cool human bodies without energy consumption. It also exhibits other desired properties, including mechanical compliance, high breathability and waterproofing. The outstanding passive-cooling capability and breathability stem from the structural engineering of multiscale porous structure in elastomer, which was achieved by simple, cost-effective, and scalable phase separation-controlled process. We also demonstrate some applications of wearable skin-interfaced bioelectronics for continuous monitoring of human vital signals and human-machine interactions. These devices are patterned by spray printing of silver nanowires on prestretched multiscale porous polystyreneblock-poly(ethylene-ran-butylene)-block-polystyrene (SEBS) substrates.

Leveraging the same versatile synthesis approach, we then introduce the synthesis of strain-insensitive conductive nanocomposite, which is enabled by well-controlled in-situ distribution of conductive nanofiller (i.e., silver nanowires) on the surface of microscale pores. The judiciously engineered structure enables substantially decreased (~50 times) percolation threshold and excellent strain-insensitivity property. The obtained porous conductive nanocomposite also exhibits outstanding breathability, conductivity, strain-insensitivity, mechanical and electrical robustness and durability.

Chapter 1

Introduction

Emerging skin-interfaced electronics have been widely researched and can find wide applications in many areas such as human health care, human-machine interface and virtual reality by continuously collecting a variety of biological signals from human body in real time (1-18). They are also referred as “epidermal electronics” (1), “smart skins” (3) or “skin-like electronics” (20), because they are designed to be highly conformable with human skin and imitate skin’s unique characteristics (4). To realize continuous and real-time monitoring, the skin-interfaced electronics need to stay on human skin for a long time. It means that besides outstanding sensing performance, high flexibility, conformability and minimal invasiveness are also highly desired to improve user comfort and minimize inflammatory reactions (30-33).

The conventional electronic materials are usually rigid, brittle, which leads to the mechanical mismatch with soft human skin (6). To overcome the disadvantages of conventional electronic materials, intrinsically stretchable polymer materials have attracted great attention (20). To achieve high breathability of skin-interfaced electronics that based on intrinsically stretchable polymer materials, two common strategies are generally employed: 1) structural engineering of polymer materials, e.g., the nanomesh structure (31, 57) and the porous structure (33, 58); 2) electrospinning or wet-spinning of nanofiber membranes (59, 60). Here, we introduce the fabrication of stretchable polymer materials with porous structure using phase separation method.

After fulfilling all these basic requirements which may affect users’ comfort physiologically and psychologically, further improvements are taken into consideration to achieve the full potential of skin-interfaced electronics.

Multifunctional porous polymer substrates

This part of study focuses on the fabrication and characterizations of the porous supporting substrates of the skin-interfaced electronics. So the primary objectives of this part are:

1) To investigate possible suitable polymer materials and fabrication methods that allow for the fabrication of porous polymer substrates.

2) To characterize the as-prepared porous polymer substrates, including pore size, thickness, breathability, stretchability, waterproof and recyclability.

3) To fabricate skin-interfaced electronics based on the porous polymer substrates and then use these electronics to collect human vital signals for health monitoring and human-machine interactions.

Conductive polymer nanocomposites

As skin-interfaced electronics require high conductivity and stretchability simultaneously, conductive polymer nanocomposites which usually have excellent mechanical and electrical properties also have attracted great attention in recent years (74). We investigated into several conductive polymer nanocomposites and pay attention to the percolation threshold, conductivity, stretchability, modulus and breathability. Lower percolation threshold can lead to higher conductivity with same amount of nanofillers used or less usage of conductive nanofillers with same electrical conductivity. However, existing conductive polymer nanocomposites either have undesirable electromechanical properties or suffer from low breathability (37, 62-77).

In this part, the aim is to fabricate breathable conductive polymer nanocomposites with substantially improved strain-insensitive properties. The primary objective of this part is:

1) To investigate possibly suitable polymer materials, nanofillers and fabrication methods, and to synthesize conductive polymer nanocomposites.
2) To characterize the conductive polymer nanocomposites, including pore size, thickness, percolation threshold, conductivity, stretchability, modulus, breathability, mechanical and electrical robustness, and durability.

Chapter 2

Multiscale porous elastomer substrates for multifunctional on-skin electronics with passive-cooling capabilities

Journal Publication Information

This article has been published in the journal “Proceedings of the National Academy of Sciences” in 2020. And I am the co-author of this article.

Authors

Yadong Xu, Bohan Sun, Yun Ling, **Qihui Fei**, Zanyu Chen, Xiaopeng Li, Peijun Guo, Nari Jeon, Shivam Goswami, Yixuan Liao, Shinghua Ding, Qingsong Yu, Jian Lin, Guoliang Huang, Zheng Yan

2.1 Introduction

Emerging on-skin electronics are designed to provide a noninvasive or minimally invasive way for long-term, real-time monitoring of a variety of biological signals from human bodies and can find wide applications in clinical health care, mobile fitness tracking, human-machine interface, and virtual reality among many others (1-18). To achieve their full potentials, most ongoing efforts center on developing 1) novel materials for on-skin electronics with outstanding mechanical pliability (e.g., flexible/ stretchable forms of inorganic materials, intrinsically soft organic materials, nanomaterials, nanocomposites) (1, 19-22); 2) biodegradable or self-healing on-skin electronics (23-26); and 3) on-skin biochemical sensors with high stability, selectivity, and sensitivity (27-29). Besides, on-skin electronics should be breathable to facilitate sweat evaporation to improve user comfort and minimize inflammation risks (30-33), be waterproof so as not to disturb users' daily activities (e.g., showering) (34), and be reusable to potentially reduce electronic waste and manufacturing cost (35).

In addition, point-of-care thermal management (e.g., joule heating, passive cooling) shows promising applications in body temperature regulations, which can improve user comfort and reduce energy consumption. On-skin electronics with joule-heating elements have been widely reported (36–38). Also, textiles, paints, and woods with passive-cooling properties have been recently developed (39–41). Besides, very recent research reveals that twisted and coiled fibers have twistocaloric cooling capabilities, which are enabled by entropy changes at various stretching states (42). However, the studies of developing on-skin electronics, which can passively cool human bodies without needing any energy consumption, are still in the infant stage. Besides, it is worth mentioning that nanofiber-based and sugar-templated porous materials have been recently used for on-skin electronics with high breathability (30–33). However, the lack of pore size control in these porous materials constrains their capabilities in enabling on-skin electronics with passive-cooling functionalities and other desired features.

In this work, we report the development of multifunctional porous on-skin electronics, which can not only exhibit outstanding passive-cooling performance but also simultaneously achieve several other attributes, such as high breathability, waterproofing, and recyclability. The unique combination of these compelling properties is rooted in multiscale porous polystyreneblock-poly(ethylene-ran-butylene) -block-polystyrene (SEBS) substrates and has not been demonstrated in state-of-the-art on-skin electronics yet. In addition, a variety of prototypic bioelectronic devices, including electrophysiological sensors, temperature sensors, hydration sensors, pressure sensors, and electrical stimulators, have been fabricated via spray printing of silver nanowires (Ag NWs) on multifunctional porous SEBS substrates. The enabled on-skin devices can perform high-fidelity measurement of various biological signals from human bodies as well as deliver electrical interventions in a programmed manner. Also, their applications in cuffless blood pressure measurement, interactive virtual reality, and human – machine interface are demonstrated.

2.2 Materials and Method

Materials

SEBS pellets (H1062) were kindly provided by Asahi Kasei. Chloroform and isopropyl alcohol (IPA) were purchased from Fisher Scientific. Silver nanowires (Ag NWs) ethanol solution (Ag NW-L50, 20mg/ml) was purchased from ACS Material. All other chemicals used were of analytical grade.

Phase Separation Method

Phase separation-based process is simple, inexpensive, and scalable, and has been used to make porous polymeric materials for surface coatings and paints, gas storage and separation, and sound damping foams among others (39, 43). The process starts with the preparation of a precursor solution of polymer and nonsolvent in solvent. Next, we just need to coat the precursor onto a substrate and dry it in air. The rapid evaporation of volatile solvent induces the phase separation of the nonsolvent from polymer to form nano/microscale droplets. Finally, the evaporation of nonsolvent droplets leads to the formation of a elastomeric substrate with hierarchical pores (39).

2.3 Synthesis of Multifunctional SEBS Substrates with Multiscale Porous Substrates

Though phase separation-based process has been used to make porous polymeric materials in many fields, research on creating multiscale porous elastomeric substrates via phase separation in a controlled fashion for multifunctional on-skin electronics is still lacking. Here, we introduce the phase separation-controlled synthesis of multifunctional SEBS substrates with multiscale porous structures (Figure 2.3.1, Figure 2.3.2).

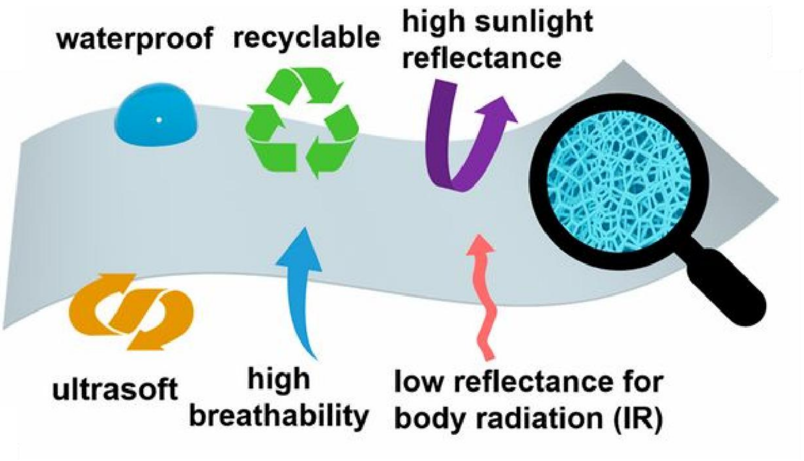

Figure 2.3.1 Schematic illustrations of the multifunctional porous SEBS substrate.

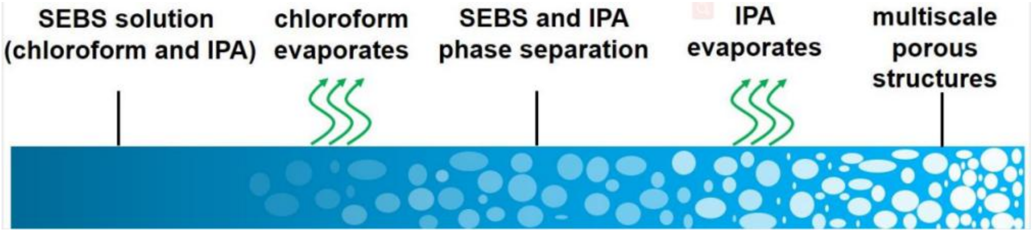

Figure 2.3.2 Schematic illustrations of the formation process of the SEBS substrates with hierarchical pores through a phase-separation-controlled method.

SEBS elastomer is adopted mainly due to its high stretchability and solution processability. We use isopropyl alcohol (IPA, boiling point, 82.6 °C) as nonsolvent and chloroform (boiling point, 61.3 °C) as solvent. The rapid evaporation of volatile chloroform will cause IPA to phase-separate from SEBS and finally the evaporation of IPA droplets will lead to the formation of the SEBS substrate with hierarchical pores. To prepare the precursor solution, we first dissolve SEBS powders in chloroform to get the SEBS stock solution (60 mg/ml), and then mix the stock solution with isopropyl alcohol at a volume ratio of 5:2, followed by sonication for 30 min. Next, we coat the precursor on an aluminum foil and dry it in air.

The optimized porous SEBS substrate exhibits ～70% porosity and is ～100 μm thick, offering outstanding passive-cooling capabilities and several other desired properties, as discussed subsequently. The optimal thickness of the porous SEBS was obtained based on the trade-off of sunlight reflectance, mid-IR reflectance, and conformability with human skin, as shown in Figure 2.3.3.

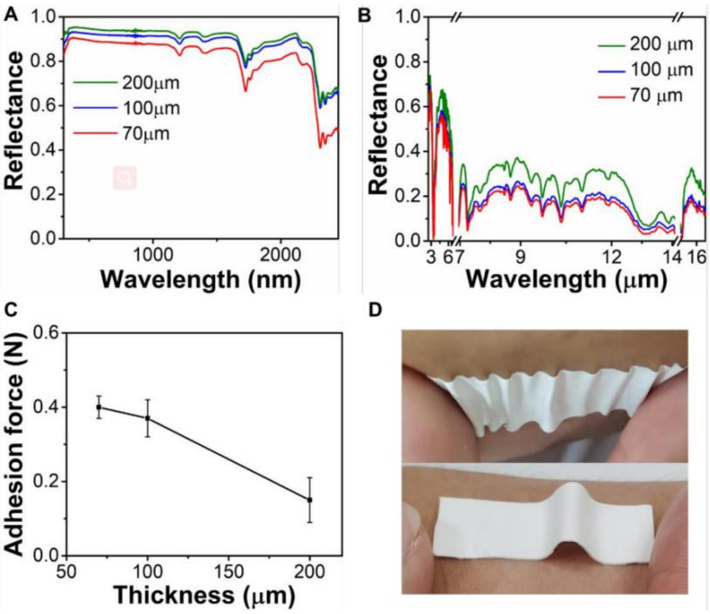

Figure 2.3.3 Thickness optimization of porous SEBS substrates based on sunlight reflectance, mid-IR reflectance, and conformability with human skin. The solar radiation reflectance (A), mid-IR radiation reflectance (B) and skin adhesion forces (C) of the porous SEBS substrates with the thicknesses of ~70 μm, ~100 μm and ~200 μm. The error bars in (C) are based on three individual measurements. (D) Optical images, indicating that the porous SEBS substrates with the thicknesses of ~140 μm (top) and ~200 μm (bottom) can easily delaminate from skin under compression. Thus, in this research, the optimal thickness (~100 μm thick) of porous SEBS was adopted for the fabrication of on-skin electronic devices based on the tradeoff of sunlight reflectance, mid-IR reflectance, and conformability with human skin.

The multiscale porous SEBS substrate indicates milky white color, as shown in Figure 2.3.4.

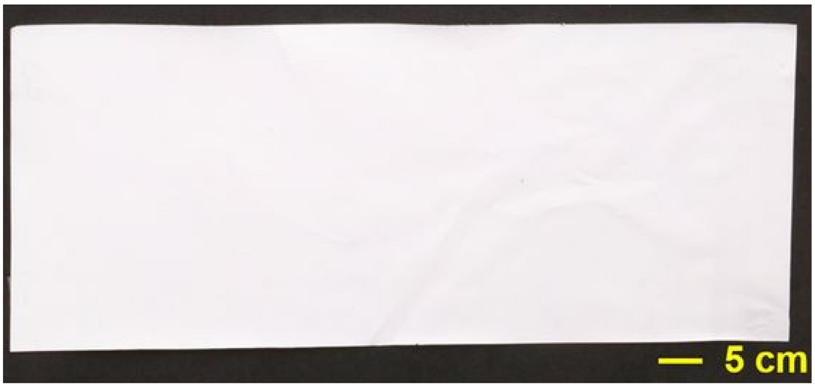

Figure 2.3.4 A photograph of the synthesized porous SEBS substrate.

The scanning electron microscope (SEM) images (Figure2.3.5 and Figure2.3.6) show the formation of fully interconnected, hierarchical pores, with characteristic sizes ranging from around 0.2 to 7 μm.

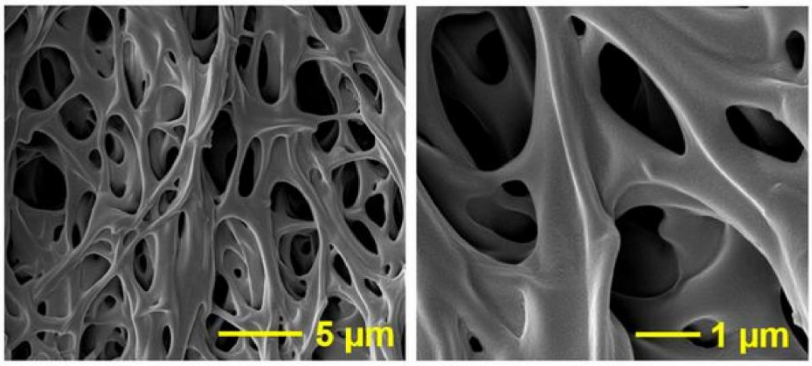

Figure 2.3.5 SEM images of the SEBS substrate showing the interconnected hierarchical pores.

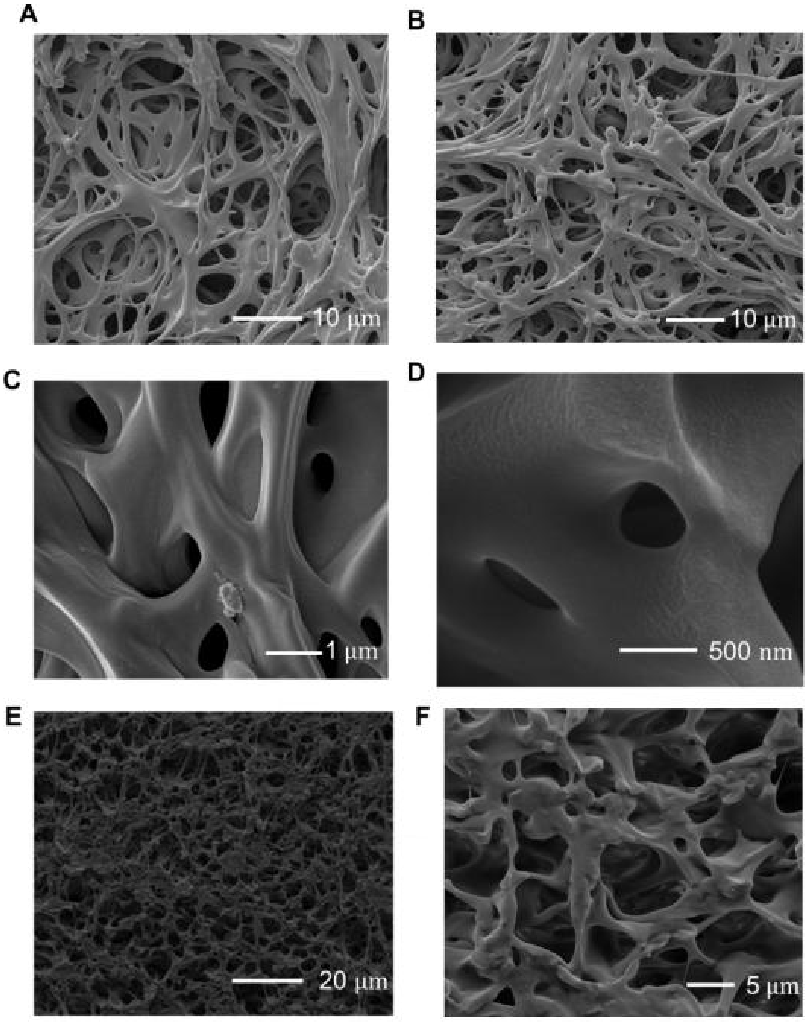

Figure 2.3.6 SEM images of the SEBS substrates with multiscale porous structures. (A-D) SEM images of the top view with different magnifications. (E, F) SEM images of cross-section view with different magnifications. SEM images show that the obtained SEBS substrates exhibit interconnected, hierarchical pores and a large amount of nanopores are embedded in the walls of micropores.

The pore size measurement, based on 300 pores, demonstrates that the number-weighted mean pore sizes are 0.61 μm for nanopores and 2.49 μm for micropores (Figure 2.3.7). As shown in Figure 2.3.8, the nano/microscale pores in the SEBS substrate can effectively backscatter sunlight (wavelength, 0.3 to 2.5 μm) but are too small to scatter human-body midinfrared (midIR) radiation (wavelength, 7 to 14 μm).

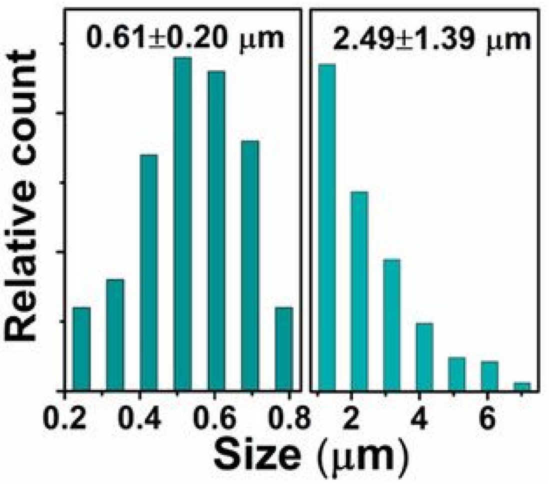

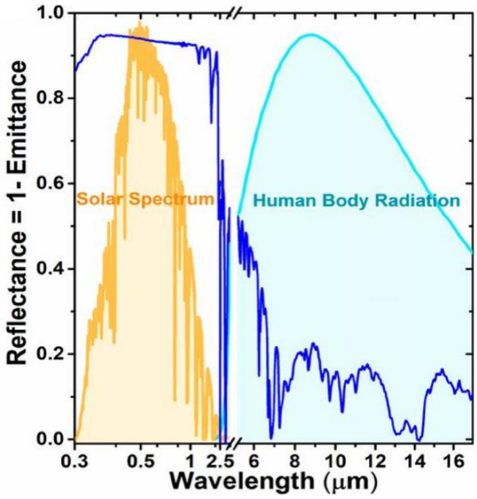

Figure 2.3.7 (Left) Pore size distributions, indicating number-weighted mean pore sizes are 0.61 μm for nanopores and 2.49 μm for micropores.

Figure2.3.8 (Right) Spectral reflectance of the porous SEBS substrate between 0.3 and 17 μm with a short break (5.1 to 5.2 μm). Human-body mid-IR radiation and normalized ASTM G173 Global solar spectrum are shaded as the light blue and orange regions, respectively, in E. Thermal mapping by IR camera and in situ measurement of skin temperatures via thermal probe.

Consequently, both a high hemispherical solar reflectance ($\bar{R}_{solar}$ = 0.92 over the range of 0.3 to 2.5 μm) and a high hemispherical IR thermal emittance ($\bar{\epsilon}_{HB}$ = 0.85 over the range of 7 to 14 μm) are achieved. Here, HB denotes human-body IR radiation. The calculations of $\bar{R}_{solar}$ and $\bar{\epsilon}_{HB}$ are provided at the end of this part (Chapter 2.3). High $\bar{R}_{solar}$ can minimize solar heat gain, and high $\bar{\epsilon}_{HB}$ can maximize radiative heat loss. Such synergistic effects can lead to outstanding daytime passive cooling. The outdoor on-body testing shows that the skin temperature covered with porous SEBS is maintained at ~6 °C lower than that of the exposed skin and ~7 °C lower than that of the skin covered with nonporous SEBS after 30 and 45 min of sunlight radiation (solar intensities, 840 $W \cdot m^{-2}$) as shown in Figures 2.3.9, 2.3.10, 2.3.11 and 2.3.12.

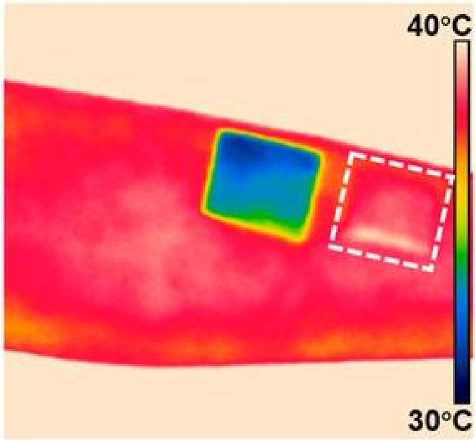

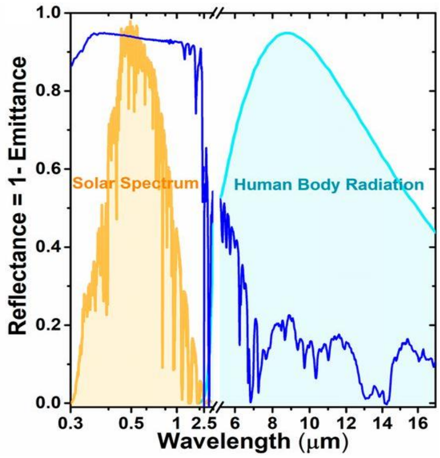

Figure 2.3.9 (right) Cooling effects (around 6 °C) induced by the porous SEBS substrate under a solar intensity of 840 $W \cdot m^{-2}$.

Figure 2.3.10 (right) Cooling effects (around 6 °C) induced by the porous SEBS substrate under a solar intensity of 840 $W \cdot m^{-2}$. Orange, red, and blue curves in G, respectively, refer to the temperatures measured from the exposed skin, skin covered with nonporous SEBS, and skin covered with porous SEBS.

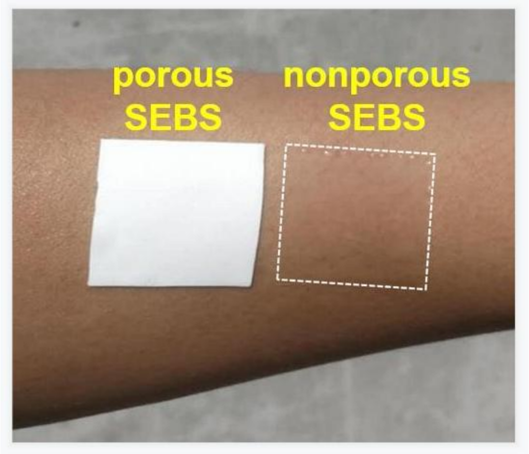

Figure 2.3.11 A photograph of porous SEBS (white) and nonporous SEBS (transparent) with same thickness attached onto the forearm of a human volunteer, corresponding to the IR thermal image shown in Figure 2.3.9.

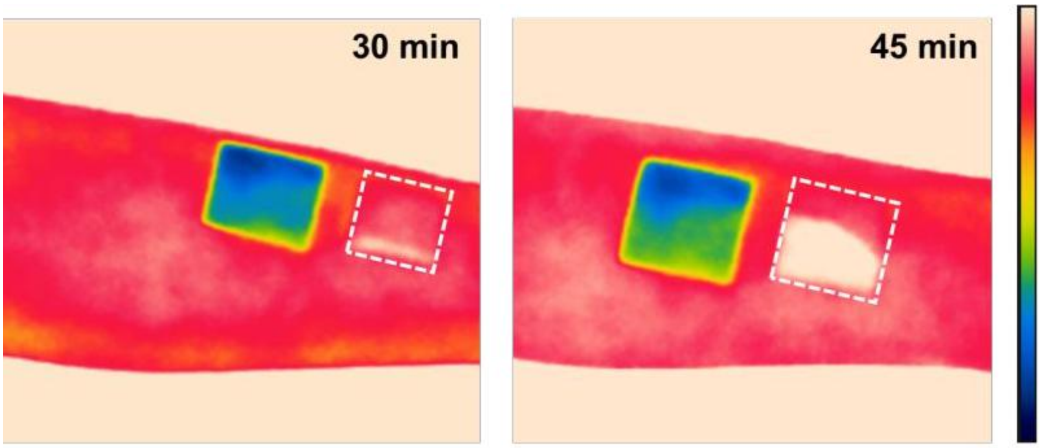

Figure 2.3.12 Thermal mapping images of porous and nonporous SEBS substrates on the human forearm after 30 and 45 mins of sunlight radiation under the solar intensity of ~840 W m^{-2}. With the increased exposed time of sunlight radiation, the skin temperature covered with porous SEBS is maintained at ~6 °C lower than that of the exposed skin and ~7 °C lower than that of the skin covered with nonporous SEBS with the same thickness.

The cooling performance of multiscale porous SEBS is comparable to those of other passive-cooling materials, which are recently reported in the literature, as shown in Table 2.3.

Table 2.3 Comparison of the passive-cooling performances of several functional materials

Materials		**Cooling performance**	**References**
Paint	P(VdF-HFP)	~6 °C	39
Wood	Delignified and densified wood	~4 °C	41
Textile	Nanoporous polyethylene	~2.7 °C	40
	NanoPE fabric	~2.3 °C	44
Elastic substrates of on-skin electronics	Multiscale porous SEBS	~6 °C	This work

In addition to superior passive-cooling capabilities, the multiscale porous SEBS substrate also exhibits a number of other desired features for on-skin electronics, including waterproofing, high breathability, recyclability, low elastic modulus, low mass density, high stretchability, and conformability. First, multiscale porous SEBS indicates enhanced hydrophobicity (water contact angle, 125 ± 4°; shown in Figure 2.3.13) compared to nonporous SEBS (water contact angle, 94 ± 2°; shown in Figure 2.3.14), mainly due to increased surface roughness stemming from porous structures.

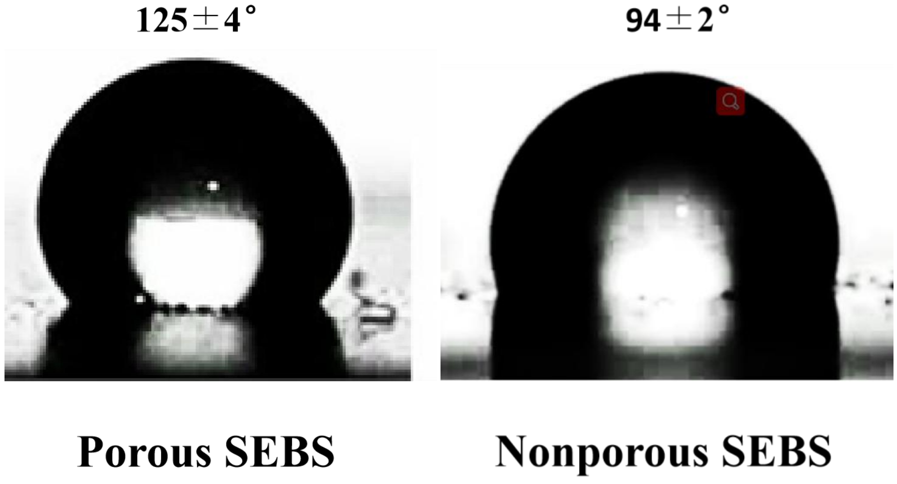

Figure 2.3.13 (left) Water contact angle of porous SEBS.

Figure 2.3.14 (right) Water contact angle measurement of nonporous SEBS, showing around 31° lower than that of porous SEBS.

As illustrated in Figure 2.3.15, multiscale porous SEBS exhibits outstanding waterproof capability because of its high hydrophobicity as well as conformal contact with skin, which is further confirmed by the on-body device testing in water.

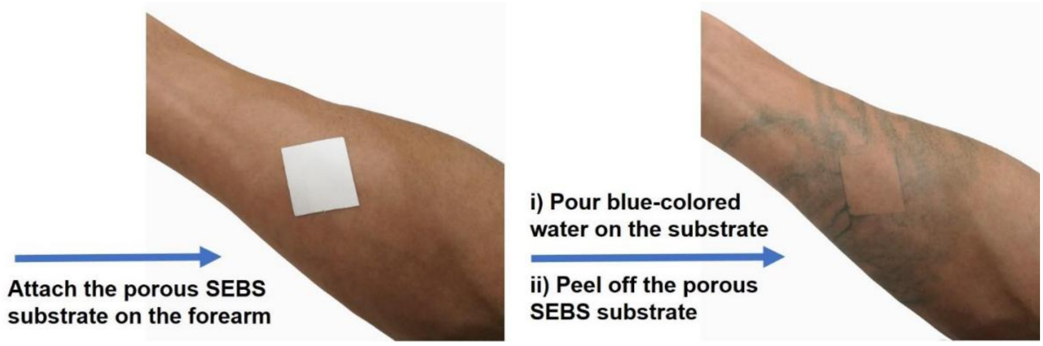

Figure 2.3.15 Waterproof test. A porous SEBS substrate was attached onto the forearm of a human volunteer. Then, the blue-colored water was poured onto the substrate. Water did not penetrate into the skin area covered by the porous SEBS substrate, indicating its outstanding waterproof capability, largely because of its high hydrophobicity and conformal contact with the skin.

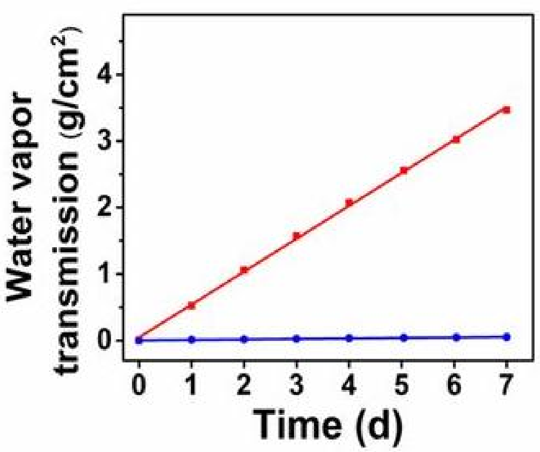

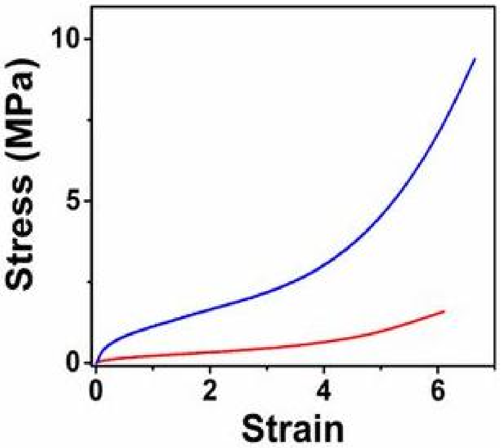

Figure2.3.16 (left) WVTRs of porous SEBS (red) and nonporous SEBS (blue) as a function of elapsed time.

Figure2.3.17 (right) Strain-stress curves of porous SEBS (red) and nonporous SEBS (blue).

Second, as shown in Figure 2.3.16, porous SEBS shows a high water vapor transmission rate (WVTR) (0.0206 $g\cdot cm^{-2}\cdot h^{-1}$) due to the interconnected hierarchical pores, which is about 69 times higher than that of nonporous SEBS with the same thickness and is comparable to recently developed, passive cooling, nanoPE fabrics (0.023 $g\cdot cm^{-2}\cdot h^{-1}$) (44). The high WVTR can expedite perspiration evaporation to improve user comfort as well as minimize inflammatory reactions caused by sweat accumulation. Third, the introduction of porous structures in the SEBS substrate can reduce the mass occupation and also create sufficient localized empty space to reduce the effective elastic modulus. Thus, the obtained porous SEBS substrate is ultrasoft and lightweight, as shown in Figure 2.3.17. Its modulus (～0.2 MPa) and mass density (～0.25 g/cm^3) are comparable to epidermis (modulus, 0.14 to 0.6 MPa; density, ～1.05 g/cm^3) and smaller than the data measured from nonporous SEBS (modulus, ～1.1 MPa; density, ～0.89 g/cm^3). The low elastic modulus can avoid skin irritation, improve user comfort, and also facilitate the formation of conformal contact with skin. The low mass density can enable lightweight on-skin electronics to alleviate physical constraints exerted on human bodies. Also, the multiscale porous SEBS substrate is highly stretchable (～600%). Besides, the enabled on-skin devices are recyclable, which is demonstrated subsequently.

Calculations of hemispherical solar reflectance and thermal emittance of the multiscale porous SEBS substrate

To efficiently scatter and reflect sunlight at all wavelength, the porous SEBS substrate needs to have high angular solar reflectance $\bar{R}_{solar}(\theta)$, defined as:

where θ is the angle between incidence angle and surface normal, λ is wavelength, $I_{solar}(\lambda)$is the ASTM G173 Global solar intensity spectrum, and $R_{solar}(\theta,\lambda)$ is the surface's angular reflectance. As the solar reflectance of the randomly oriented, porous structures are demonstrated to be almost independent on angles, thus $\bar{R}_{solar}(\theta,\lambda)$ and $\bar{R}_{solar}(\theta)$ is regarded as the same.

To maximize heat dissipation from human body to the environment, the SEBS substrate needs to have high IR thermal emittance $\bar{\epsilon}$ over the range where human body emits heat energy, defined as:

$$\bar{\epsilon}_{HB} = \frac{\int_{7\mu m}^{14\mu m} I_{BB}(T,\lambda)\epsilon(T,\lambda)d\lambda}{\int_{7\mu m}^{14\mu m} I_{BB}(T,\lambda)d\lambda}$$

where the 7-14 μm bounds represent the main range of human body heat radiation, $I_{BB}(T,\lambda)$ is the spectral intensity emitted by a blackbody at temperature (25 °C) and $\epsilon(T,\lambda)$ is the surface's spectral hemispherical thermal emittance. $I_{BB}(T,\lambda)$ is defined as:

$$I_{BB}(T,\lambda) = \frac{2hc^2}{\lambda^5}\frac{1}{e^{hc/(\lambda k_B T)-1}}$$

Where h is Planck's constant, k_B is the Boltzmann constant, is the speed of light.

2.4 Spray Printing of Ag NWs on Prestretched Multiscale Porous SEBS Substrates

Ideally, on-skin electronics should be one-time use and disposable to minimize infection risks. Thus, it is highly desirable to achieve scalable patterning of electronic components on supporting substrates to potentially lower manufacturing cost. The solution-printing-based fabrication offers a simple, cost-effective, high-throughput way for patterning devices on flexible supporting substrates (5, 45, 46). In this research, we fabricated a variety of prototypic on-skin bioelectronic devices via spray printing of Ag NWs on multiscale porous SEBS substrates. Here, Ag NWs (diameter, 50 nm; length, 100 to 200 μm) are used mainly because they exhibit outstanding mechanical compliance and high electrical conductivity, and can be easily produced in a large quantity (37).

As illustrated in Figures 2.4.1 and 2.4.2(A), we first investigate the spray printing of open-mesh, serpentine-like layouts of Ag NWs on prestretched multiscale porous SEBS (uniaxial prestrain, 150%), which can serve as the basic building blocks for a variety of bioelectronic devices as demonstrated in Figure 2.4.2(B).

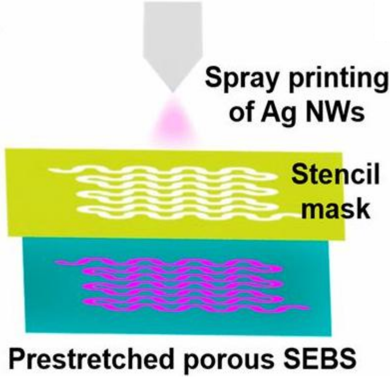

Figure 2.4.1 A schematic diagram of the spray printing of Ag NWs onto prestretched porous SEBS through a stencil mask.

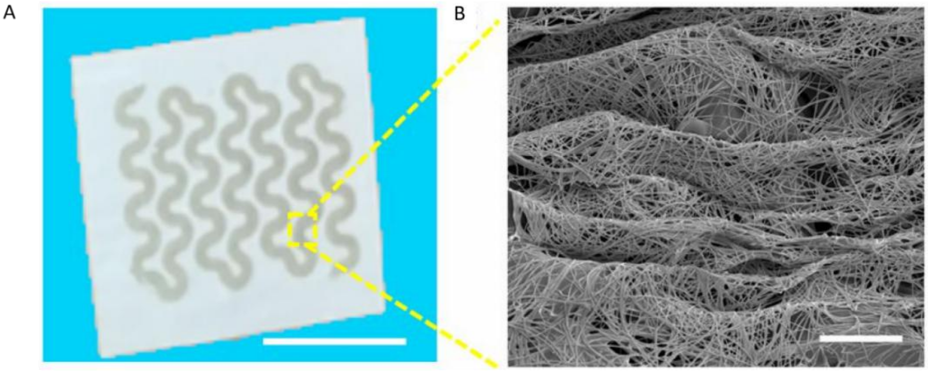

Figure 2.4.2 (A) A photograph of a serpentine-like conductive trace, made of spray-printed Ag NWs, on porous SEBS. (Scale bar: 1 cm) (B) SEM image, showing the formation of microscale wavy structures of Ag NWs networks with underneath porous SEBS (Scale bar: 5 μm).

After the spray printing, releasing the prestretched substrate leads to the formation of microscale wavy structures of Ag NWs networks with underneath porous SEBS (Figure 2.4.2(B) and Figure 2.4.3).

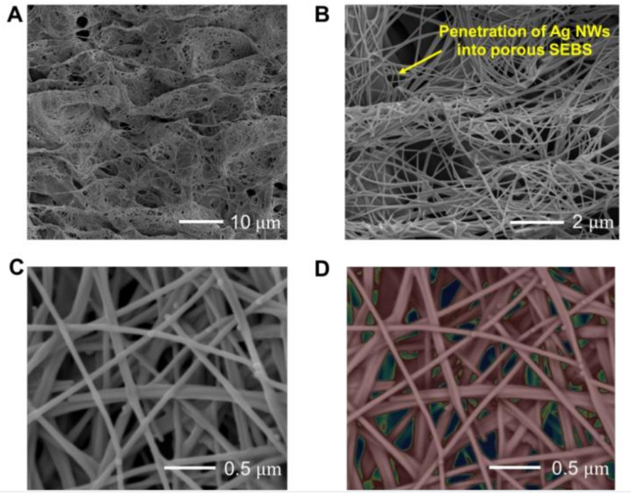

Figure 2.4.3 SEM images of spray-printed Ag NWs on porous SEBS. (A, B) SEM images of spray-printed Ag NWs on porous SEBS, indicating the formation of microscale wavy structures as well as strong bonding interface because of the penetration of Ag NWs into the pores. The robust interfacial adhesion is further confirmed via the cycling bending and stretching tests (Figure 2.3.15). The high-magnification SEM image of Ag NWs networks (C) and the corresponding simulated SEM image with Wolfram Mathematica (D), which are used for the estimation of the thickness, surface coverage and porosity of the spray-printed Ag NWs networks.

The spray-printed Ag NWs patterns (～200 nm thick) show high electrical conductivity (11,000 S/cm). Also, the wavy structures endow the printed Ag NWs with outstanding electromechanical properties. For example, both bending and stretching produce small effects on their electrical properties (Figures 2.4.4).

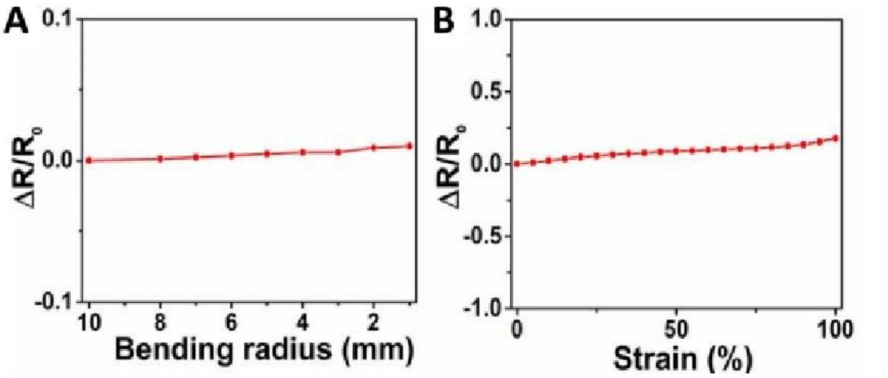

Figure 2.4.4 Variations in electrical resistance of the Ag NWs patterns on porous SEBS as a function of bending radius and strain.

In particular, the electrical resistance shows a negligible change (～1%) at a bending radius of 1 mm and increases ～17% under 100% uniaxial strain. By contrast, the natural deformations of human skin are up to 50 to 80%. Also, the spray-printed Ag NWs exhibit high durability and cyclability (Figures 2.4.5). After 1,000 cycles for a bending radius of 1 mm, the resistance only increases ～1.7%. Similarly, only ～6% resistance increase is observed after 2,000 cycles of stretching test under 50% uniaxial strain.

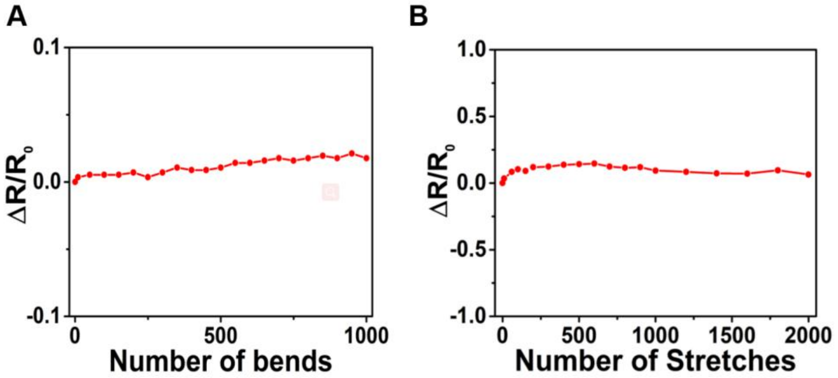

Figure 2.4.5 Normalized electrical resistance changes under the cycling bending and stretching tests. (A) 1,000 cycles of bending test under the bending radius of 1 mm. (B) 2,000 cycles of stretching test under the uniaxial strain of 50%. Notably, after 1,000 cycles for a bending radius of 1 mm, the resistance only increases ~1.7%. Similarly, only ~6% resistance increase is observed after 2,000 cycles of stretching test under 50% strain.

Most importantly, the integration of open-mesh, serpentine-like patterns of Ag NWs exhibits negligible effects on the passive-cooling capability, breathability, and elastic modulus of multiscale porous SEBS substrates (Figures 2.4.6).

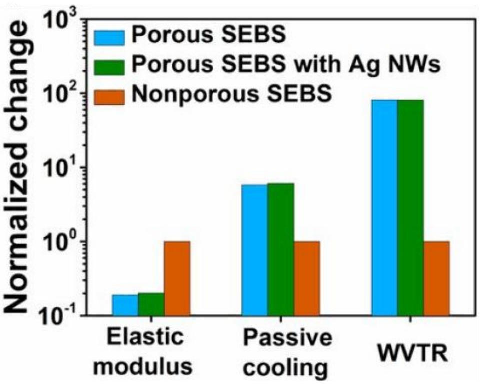

Figure 2.4.6 Comparisons of nonporous SEBS, porous SEBS, and porous SEBS with Ag NWs patterns, in terms of water vapor transmission rate (WVTR), passive-cooling capability, and elastic modulus, indicating significant improvement of porous SEBS over nonporous SEBS and negligible changes after Ag NW printing.

This is largely because porous SEBS is the major component of the obtained sample. Specifically, the Ag NWs patterns only occupy ～1% by weight and ～0.2% by thickness of the entire sample and account for ～16% surface coverage on the side that directly touches the skin. It is worth noting that Ag NWs can not only reflect IR radiation to warm human body but also enhance the surface emissivity to efficiently dissipate heat back to the environment (47, 48). The coating of Ag NWs serpentine patterns has a trivial effect on the cooling performance of porous SEBS, indicating ～6 °C and ～6.3 °C temperature drops, respectively, before and after Ag NWs printing. This is mainly because 1) Ag NWs patterns only occupy a small portion of the surface area of the sample (～16%); and 2) Ag NWs are outstanding thermal conductors, which can enable efficient heat transfer between skin and multiscale porous SEBS (Figure 2.4.7).

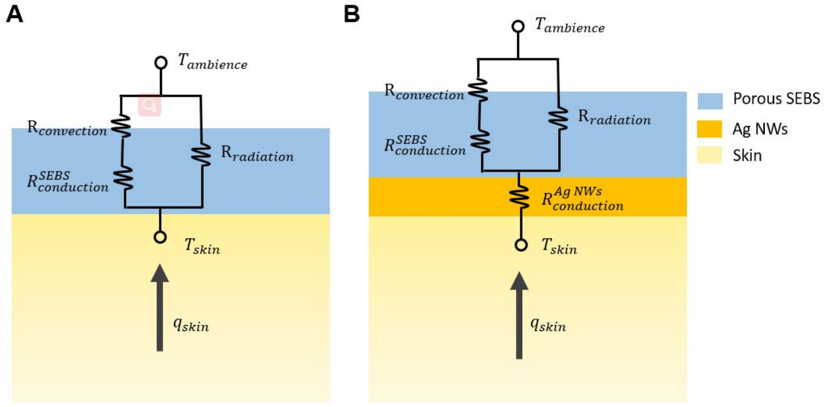

Figure 2.4.7 Thermal circuit model when porous SEBS forms conformal contact with human skin.

In addition, the obtained sample can form robust, conformal contact with the skin (Figure 2.4.8) mainly due to its low effective modulus (~0.2 MPa) and small thickness (~100 μm). As shown in Figure 2.4.9, adhesion peel test indicates porous SEBS exhibits a significantly higher skin adhesion force than that of its nonporous counterpart with the same thickness, which is comparable to the data measured from ultrathin epidermal electronic systems (49).

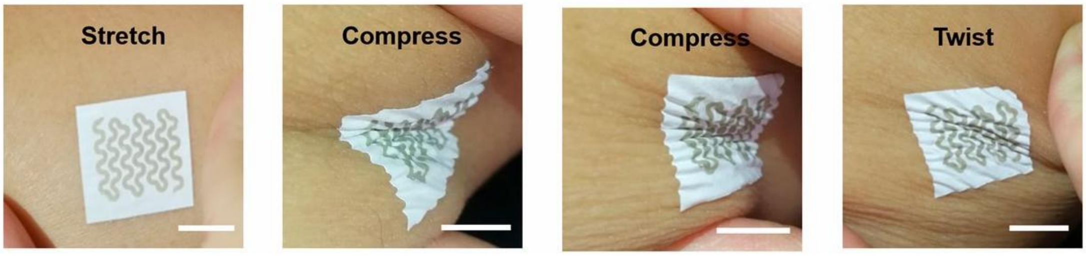

Figure 2.4.8 Photographs, showing the formation of the robust conformal contact between the sample and the skin. Mechanical deformations, including stretching, compressing, and twisting, do not induce delamination (Scale bars: 1 cm)

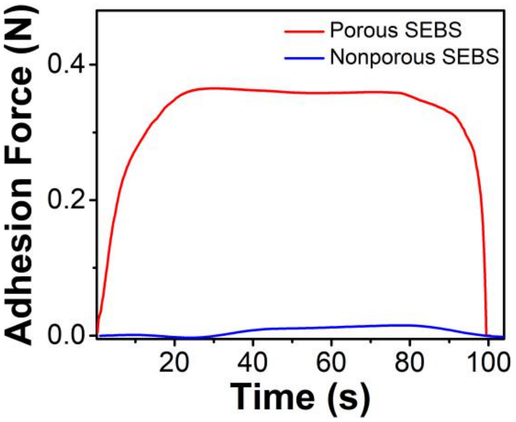

Figure 2.4.9 Peel adhesion test of porous and nonporous SEBS substrates (~100 μm thick) from the human forearm.

2.5 Multimodal On-Skin Electronics Based on Multiscale Porous SEBS and Spray-Printed Ag NWs

Human bodies usually undergo complex physiological changes in daily activities and can naturally emanate a broad spectrum of biological information. Thus, it is highly desirable to enable on-skin electronics with multimodalities (i.e., incorporate multiple sensors and stimulators together) to obtain a complete picture of the body's physiological status as well as deliver required interventions. Here, we demonstrate porous, multimodal on-skin bioelectronic patches, consisting of electrophysiological (i.e., biopotential) sensors, temperature sensors, hydration sensors, and electrical stimulators (Figure 2.5.1 and Figure 2.5.2), which are fabricated via spray printing of Ag NWs on multiscale porous SEBS substrates. The enabled porous on-skin devices show comparable electrical performances with conventional, rigid, nonporous ones, as described below.

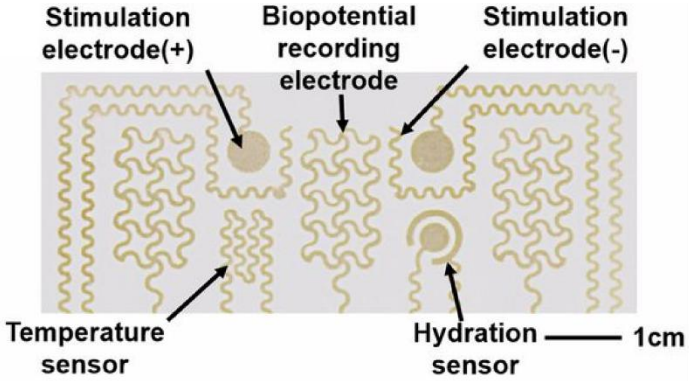

Figure 2.5.1 A photograph of the multimodal on-skin electronic patch, which was fabricated via the spray printing of Ag NWs on the multifunctional porous SEBS substrate.

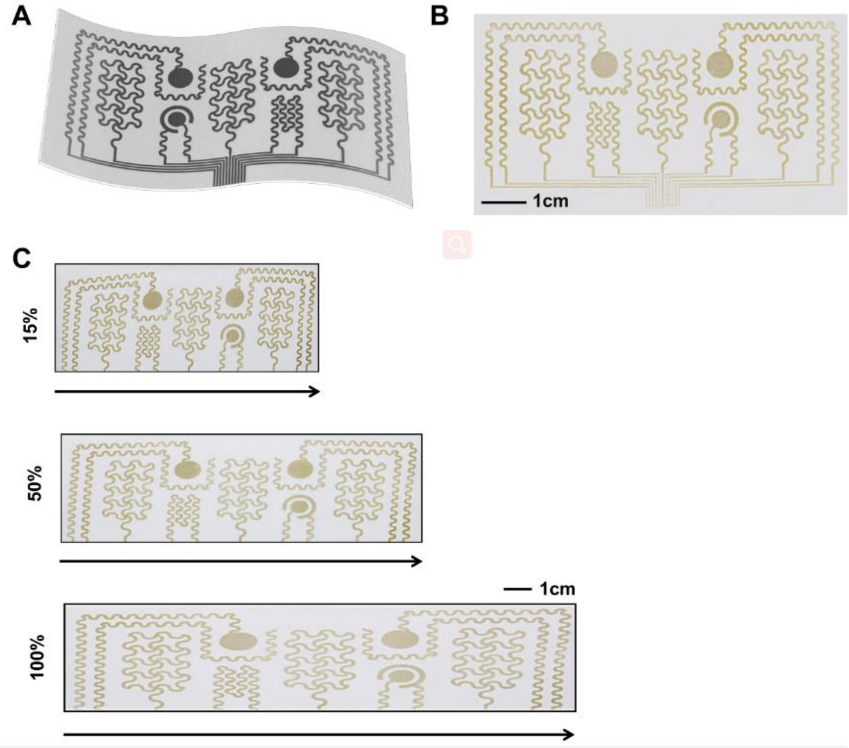

Figure 2.5.2 The obtained multimodal on-skin electronic patch.

The electrophysiological sensor consists of reference, ground, and measurement electrodes of Ag NWs. As shown in Figure 2.5.3 and Figures 2.5.4-2.5.10, the obtained on-skin electrophysiological sensor can be laminated onto the different locations of human bodies to record alpha rhythm (from forehead), electrocardiograms (ECGs) (from chest), and electromyograms (EMGs) (from forearm, flexor carpi radialis muscle; face, masseter muscle; and back and neck, trapezius muscle). The contact impedance is ~33 kΩ at 100 Hz, comparable to conventional silver/ silver chloride (Ag/AgCl) gel electrodes (~21 kΩ at 100 Hz) (Figures 2.5.11).

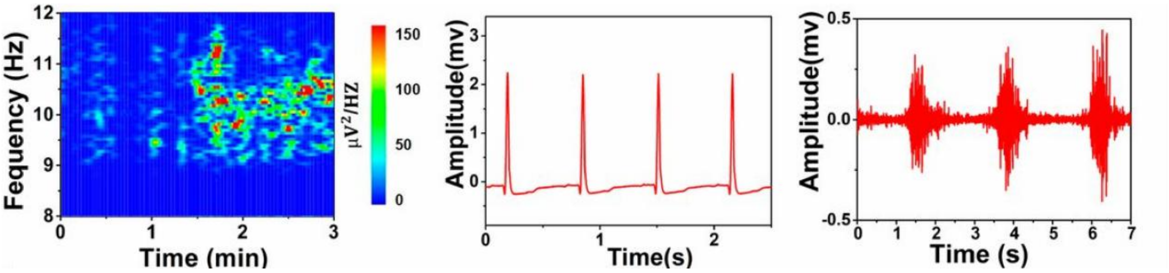

Figure 2.5.3 Recorded alpha rhythm (Left), ECG signals (Middle), and EMG signals (Right).

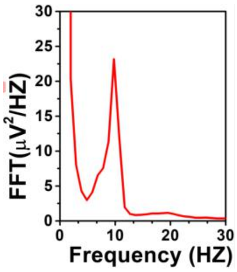

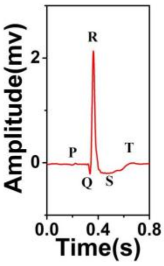

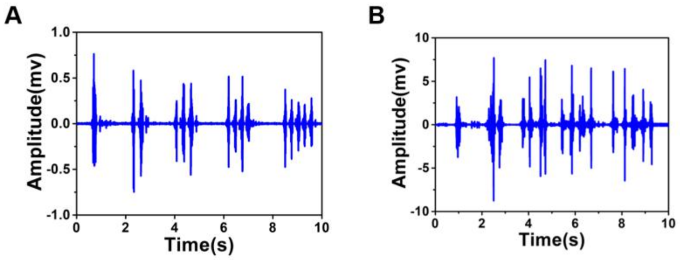

Figure 2.5.4 (left) Fast Fourier transform (FFT) analysis of the electroencephalogram (EEG) signal recorded from the forehead of a volunteer when the volunteer was asked to keep the eyes open for approximately 90 s and then close the eyes for 90 s, showing that the alpha rhythm is centered at ~10 Hz.

Figure 2.5.5 (middle) The magnified ECG signal from Figure 2.5.3, indicating clearly visible P-wave, QRS complex, and T-wave.

Figure 2.5.6 (right) Recorded EMG signals when the volunteer was asked to clench the jaw (A) and nod the neck (B) for once, twice, three times, four times, and five times. During the testing, the porous on-skin devices were attached onto the volunteer’s face (muscle: Masseter) in A and back neck (muscle: Trapezius) in B, respectively, for EMGs recording.

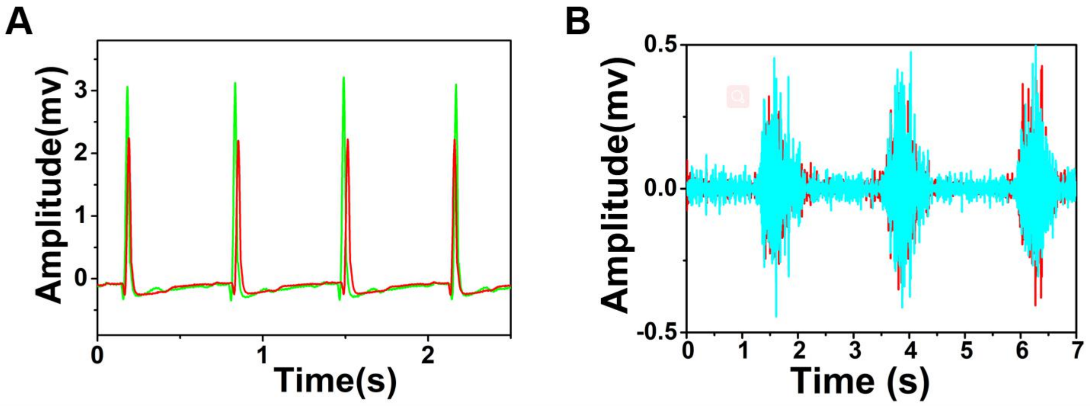

Figure 2.5.7 ECGs and EMGs recorded using the porous on-skin devices (red in A and B; SNR for ECGs: ~22.7 dB; SNR for EMGs: ~20.7 dB) and commercial Ag/AgCl electrodes (green in A and blue in B; SNR for ECGs: ~20.5 dB; SNR for EMGs: ~22.4 dB).

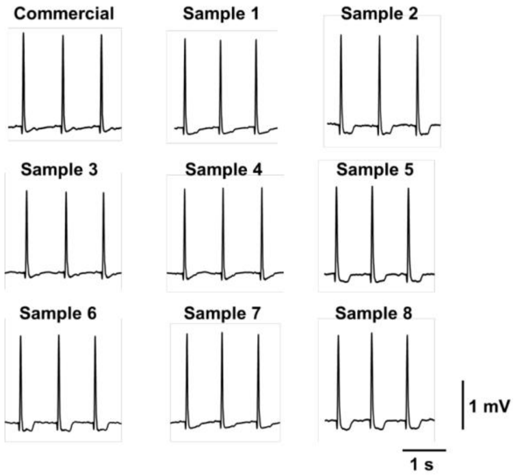

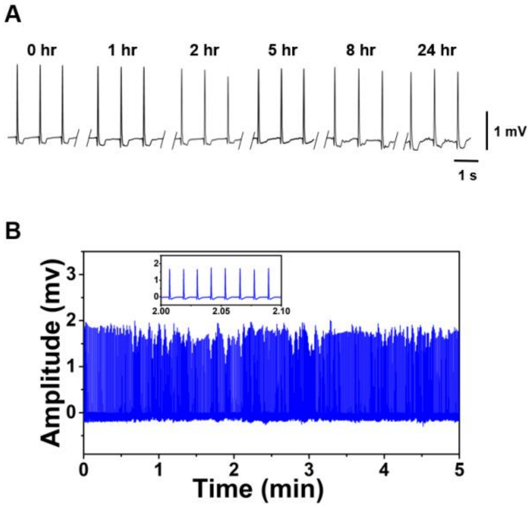

Figure 2.5.8 (left) ECG signals recorded with commercial Ag/AgCl gel electrodes and eight randomly selected porous on-skin devices, demonstrating high reproducibility.

Figure 2.5.9 (right) Long-term and continuous ECGs recording using the porous on-skin device from the chest of a human volunteer, indicating high stability. (A) Recorded ECG signals after the volunteer wore the device for 0 h, 1 h, 2 h, 5 h, 8 h, and 24 h. (B) Continuous ECGs measurement for 5 min.

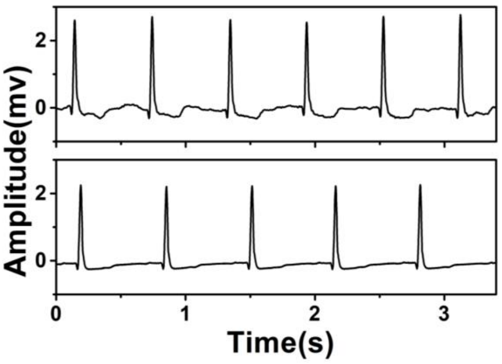

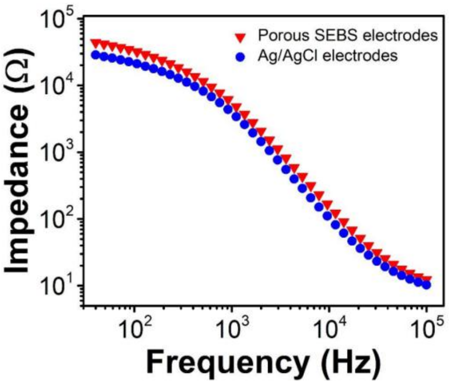

Figure 2.5.10 (left) ECG signals measured by the porous on-skin device from the chest of a volunteer before doing exercise (bottom) and after running one kilometer with a high moisture level (top), demonstrating the trivial effects of sweat on the device performance.

Figure 2.5.11 (right) Impedance of the skin/electrode interface. Commercial Ag/AgCl electrode is used as reference. A pair of our porous electrophysiological sensors and a pair of Ag/AgCl electrodes (Kendall™ 530 series, Cardinal Health) were laminated onto human forearm at the same location after cleaning the forearm with alcohol swabs. The size of our electrode and the Ag/AgCl electrode is 20 mm × 11 mm and the center-to-center distance is 15 mm.

Both ECGs and EMGs recorded using the porous on-skin sensors exhibit quantitively comparable patterns with those measured by Ag/AgCl gel electrodes (Figure 2.5.7). Specifically, the EMGs recorded with the porous on-skin devices indicate the signal-to-noise ratio (SNR) of ~20.7 dB. As a comparison, the SNR of the EMGs measured with Ag/AgCl electrodes is ~22.4 dB. Besides, the device fabrication process reported in this research is highly reproducible, as confirmed by the highly repeatable ECGs recording from 8 randomly selected devices (Figure 2.5.8). Also, the long-term and continuous ECG measurement (Figure 2.5.9) indicates the high device stability. In addition, due to the porous structures of enabled on-skin devices, the heavy skin perspiration and high levels of moisture have the trivial effects on the device performance (Figure 2.5.10). It is known that electrical stimulations can alleviate pain and are also useful for rehabilitation and prosthetic motor control (50, 51). As shown in Figure 2.5.12, monophasic square pulses of 2 mA (10 Hz; pulse duration, 25 ms) is applied through the bipolar stimulation electrodes of Ag NWs to the forearm. The recorded EMG signals, from the muscle (flexor carpi radialis) contractions induced by the electrical stimulations, exhibit a good alignment with the stimulation signals, indicating the capability of delivering required electrical interventions in a programmed manner. Furthermore, we demonstrate the application of the enabled on-skin electrophysiological sensors in the control of a soft robotic hand, which is based on graphene electrothermal actuators. Specifically, 2 on-skin electrophysiological sensor patches were laminated, respectively, on the extensor pollicis longus and extensor pollicis brevis muscles, and flexor carpi radialis muscle of a human volunteer to record EMGs. The EMG signals acquired from the extensor pollicis longus and extensor pollicis brevis muscles were used to control the soft robotic thumb, whereas the EMG signals recorded from the flexor carpi radialis muscle were used to control another 4 fingers. As shown in Figure 2.5.13, the soft robotic hand can successfully identify and emulate human hand motions. The response time is ~8 s, the bending angle is ~360°, and the bending curvature is ~1.4 cm^{-1}.

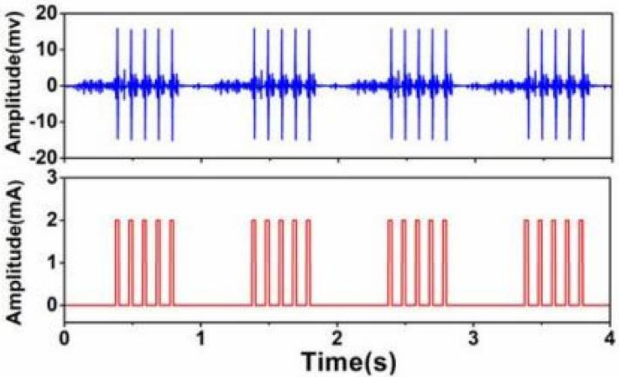

Figure 2.5.12 Recorded EMG signals (Top) during electrical stimulations (Bottom).

Figure 2.5.13 Photographs, indicating the control of a soft robotic hand via EMGs recording.

In addition, the enabled on-skin temperature sensors and hydration sensors also demonstrate high performance (Figures 2.5.14-2.5.16). The on-skin temperature sensor consists of an Ag NW conductive trace. The temperature coefficient of resistance is 2.14×10^{-3} °C^{-1} (Figure 2.5.17) and provides the basis for the on-skin thermal measurement. Here, a hot pad was applied to warm the skin to ~45 °C before the test. Then an ice bag was used to accelerate cooling during the test. Figure 2.5.14 indicates that the skin temperatures measured using the on-skin temperature sensor nearly overlap with the ones recorded with a commercial thermocouple. The on-skin hydration sensor consists of a coaxial dot-ring electrode of Ag NWs and can measure skin impedance, reflecting skin hydration levels. Figure 2.5.15 shows the skin impedance variations as a function of frequency at different hydration levels, indicating the correlations between skin impedance and hydration levels. The on-skin hydration sensor was calibrated using a commercial skin moisture sensor and was used to examine the natural decay of skin hydration levels after applying moisturizing lotion. The results recorded by the on-skin hydration sensor agree well with the data obtained from a commercial hydration sensor (Figure 2.5.16). The calculated SD is 1.8% based on a sample size of 16.

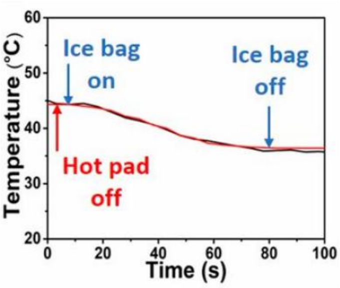

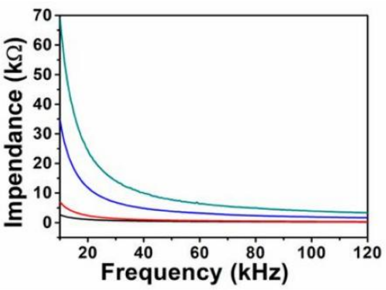

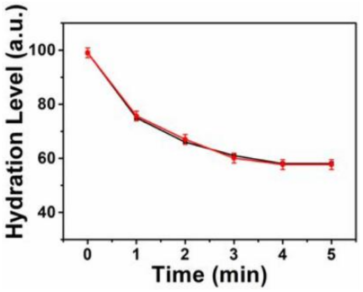

Figure 2.5.14 (left) Recorded skin temperatures (blue), which nearly overlaps with the data measured from a thermocouple (red). Here, a hot pad was applied to warm the skin to ～45 °C before the test. Then an ice bag was used to accelerate cooling during the test.

Figure 2.5.15 (middle) Impedance variations as a function of frequency at the hydration levels of 99% (green), 88% (blue), 70% (red), and 67% (black).

Figure 2.5.16 (right) Recorded skin hydration decay as a function of time after applying moisturizing lotion (red), which agrees well with the data measured from a commercial skin moisture sensor (black).

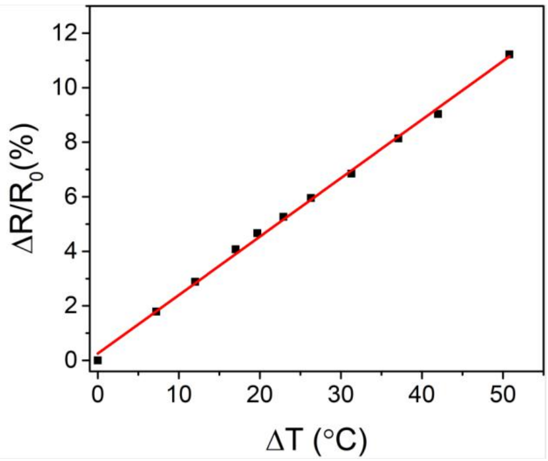

Figure 2.5.17 Resistance variations of the Ag NWs-based on-skin temperature sensor as a function of temperature change. The temperature coefficient α, which is described as: $\frac{\Delta R}{R_0} = \alpha \cdot \Delta T$, is calculated to be $0.00214\ ^{\circ}C^{-1}$.

2.6 Demonstrations of Waterproof, Recyclability and Cuffless Blood Pressure Measurement

As demonstrated in Figures 2.6.1, the enabled on-skin electronic patch is waterproof and can operate well in water. During the testing, the volunteer was asked to wear the on-skin device on the forearm and then fully submerged the forearm in water. After 20 min, the volunteer was asked to squeeze the fist in water once, twice, 3 times, 4 times, and 5 times. Remarkably, the recorded EMG signals are clearly distinguishable from the baseline noise and are comparable to the data recorded in air.

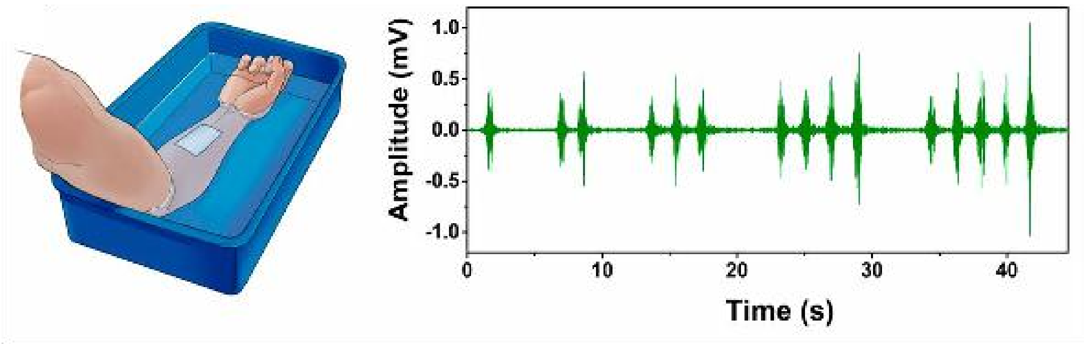

Figure 2.6.1 EMGs recording when the on-skin device was fully submerged in water.Since the Ag NWs side is laminated onto human skin, the conformal contact between the porous SEBS substrate and skin allows the encapsulation of Ag NWs, blocking their direct contact with water, thus providing the waterproof capability of the Ag NWs even in water.

Moreover, our on-skin electronics based on multiscale porous SEBS substrates and Ag NWs are recyclable. By contrast, silicone elastomer (e.g., polydimethylsiloxane), one widely used substrate material for on-skin electronics, is not dissolvable after curing and thus is not recyclable. As shown in Figure 2.6.2(A), we can dissolve the obtained multifunctional on-skin electronic patch in chloroform and then separate SEBS with Ag NWs via centrifugation for reuse. The porous on-skin devices made of reused SEBS and Ag NWs exhibit comparable performances with the ones made of fresh materials (Figure 2.6.2(B)).

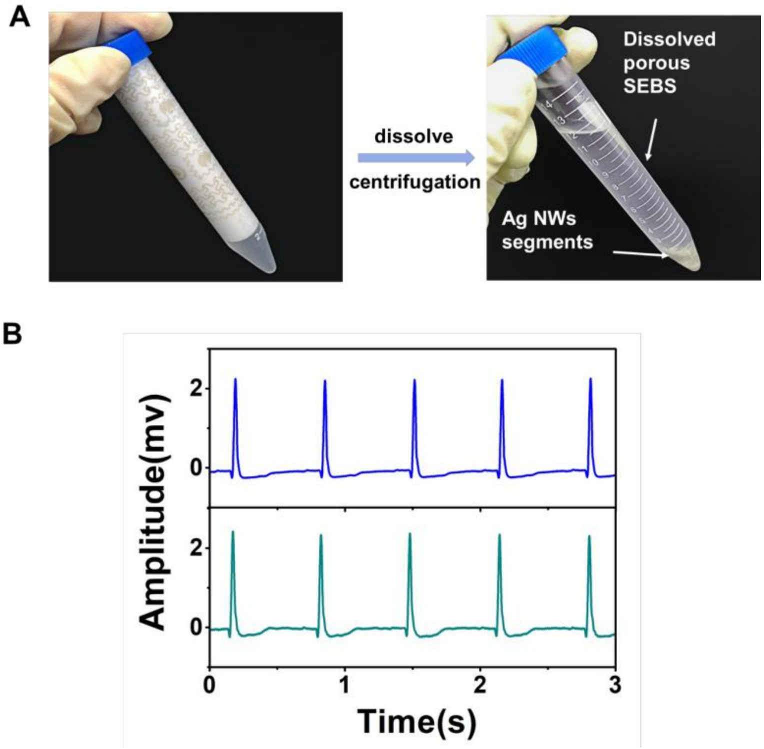

Figure 2.6.2 Recyclability of porous SEBS composite. (A) The recycling process of the multifunctional on-skin electronic patch. (B) ECGs recorded using the on-skin device made of fresh SEBS and Ag NWs (bottom) and the one made of reused materials (top).

Continuous cuffless monitoring of blood pressures can provide a wealth of information for the quantitative evaluation of various cardiovascular diseases as well as general health (52-54). In this research, we demonstrate the application of multiscale porous SEBS-based on-skin devices in continuous cuffless measurement of beat-to-beat blood pressures via concurrent recording of ECGs and arterial pulse waveforms (Figures 2.6.3-2.6.5).

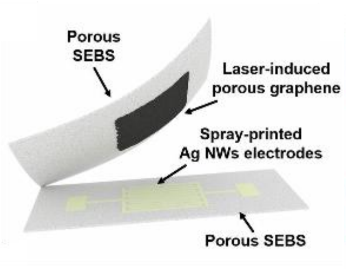

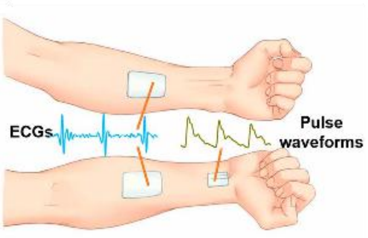

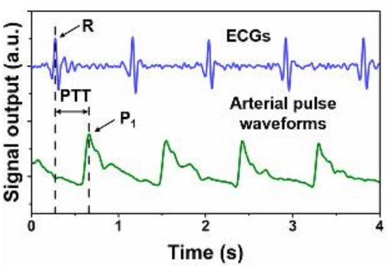

Figure 2.6.3 (left) A schematic diagram of the assembled piezoresistive on-skin pressure sensor.

Figure 2.6.4 (middle) Schematic illustrations of the simultaneous recording of ECG signals and arterial pulse waveforms for blood pressure monitoring.

Figure 2.6.5 (right) Recorded concurrent ECG signals and arterial pulse waveforms with the pulse transit time (PTT) indicated.

The ECG measurement was performed using the aforementioned porous on-skin electrophysiological sensors. The pulse waveforms monitoring was conducted with a piezoresistive on-skin pressure sensors, consisting of laser-induced porous graphene (55) as sensing elements, a pair of interdigital electrodes of spray-printed Ag NWs, and top encapsulation and bottom supporting layers of multiscale porous SEBS (Figure 2.6.3). As demonstrated in Figure 2.6.6, the assembled pressure sensor indicates high sensitivity, high repeatability, and quick response time (~36 ms). For instance, it can monitor a minute pressure change caused by the stepwise addition of a 10-μL water droplet and exhibits negligible change after repetitive pressure loading for 1,000 cycles.

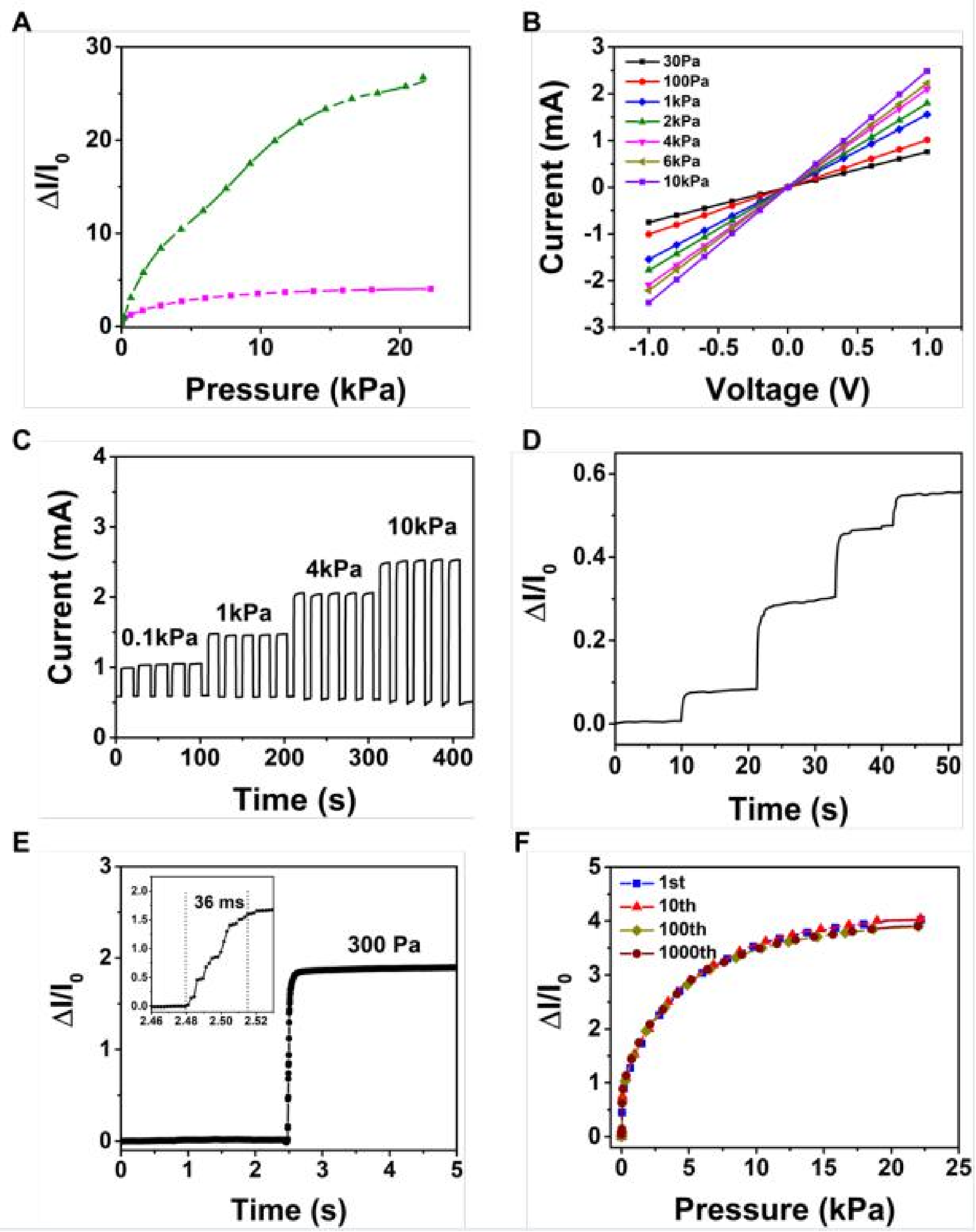

Figure 2.6.6 Systematic characterizations of the assembled piezoresistive on-skin pressure sensor. (A) Relative change in the current of the pressure sensors, made of laser-induced porous graphene (LIG) with different sheet resistances (green: ~ 1M Ω /sq red: ~ 10 k Ω /sq), under different pressures. As indicated in A, the pressure sensors, made of LIG with a higher sheet resistance (green: ~1M Ω /sq), is more sensitive and can pick up a lot of noises during the on-skin measurement of pulse waveforms. Thus, in this research, LIG with the sheet resistance of ~10 k Ω /sq is adopted for the fabrication of the on-skin pressure sensor. (B)

Current-voltage curves of the pressure sensor measured under various pressures ranging from 30 Pa to 10 kPa. (C) Dynamic responses of the pressure sensor under loading/unloading cycles for different pressures, showing a stable and immediate response. (D) Relative change in the current with the subtle increase of the pressures via stepwise addition of a 10 μl of water droplet. (E) Response time of the pressure sensor with a loading pressure of 300 Pa, indicating a quick response time of ~36 ms. (F) Relative change in the current of the pressure sensor under repetitive loading cycles, demonstrating the excellent repeatability.

As illustrated in Figure 2.6.4, the continuous, simultaneous recording of ECGs and pulse waveforms was conducted by applying 2 on-skin electrophysiological sensors on the forearms and one on-skin pressure sensor on the wrist. The obtained results are provided in Figure 2.6.5. The beat-to-beat diastolic blood pressures and systolic blood pressures are extracted using a pulse transit time (PTT) method (Figure 2.6.7) (56). The PTT is the time interval between the “R” peak of the ECG signal and the P1 point of the pulse waveform within the same cardiac cycle (Figure 2.6.5). Notably, the measured beat-to-beat diastolic blood pressures and systolic blood pressures using our porous on-skin devices are in good agreement with the results measured from a commercial sphygmomanometer (Figure 2.6.8).

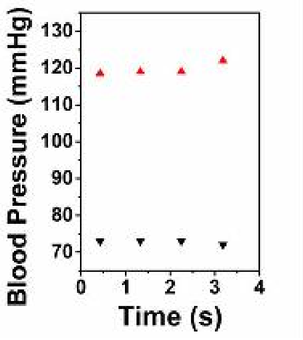

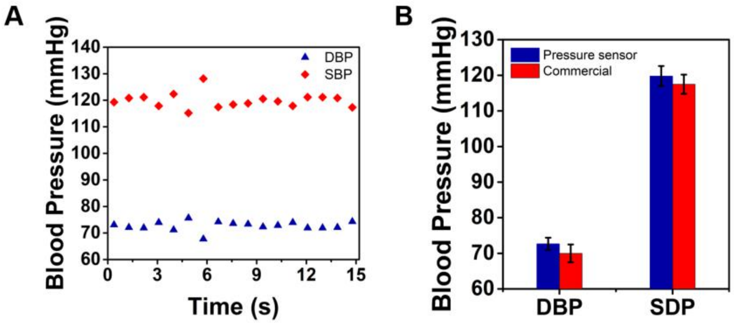

Figure 2.6.7 (left) The calculated beat-to-beat systolic blood pressures (red) and diastolic blood pressures (black) based on the PTT method.

Figure 2.6.8 (right) Beat-to-beat blood pressure measurement. (A) Beat-to-beat systolic blood pressures (SDP) and diastolic blood pressures (DBP) extracted the pulse transmit time (PTT). (B) Comparisons of the DBP and SDP measured using the on-skin devices with the data measured from a commercial sphygmomanometer. The standard deviations of the blood pressures measured with the commercial sphygmomanometer are based on 6 readings.

2.7 Control of Virtual Character and a Quadcopter via Real-Time EMGs Recording

Furthermore, we demonstrate the applications of the enabled porous on-skin electronics in interactive virtual reality and realtime control of a quadcopter via high-fidelity EMG recording. The flowchart is provided in Figure 2.7.1. Specifically, the onskin EMG sensors are laminated on the forearms (muscle, flexor carpi radialis) to collect the relevant EMG signals when the volunteers perform 4 different bimanual gestures: bending wrists inward, bending wrists to the left, bending wrists to the right, and bending wrists outward.

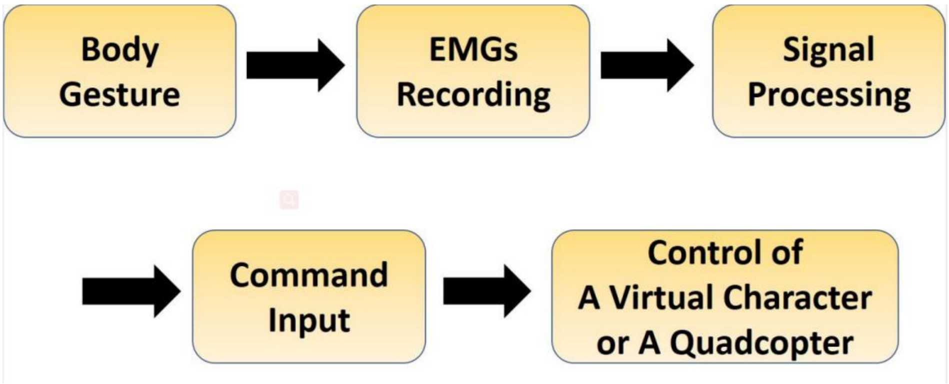

Figure 2.7.1 The flow chart for the control of a virtual character or a quadcopter via real-time EMGs recording.

As shown in Figure 2.7.2, the root-meansquare (RMS) values of the recorded EMG signals exhibit characteristic patterns and can be classified into 4 distinct control signals, termed A, B, C, and D. The classification accuracy is evaluated and summarized in a confusion matrix (Figure 2.7.3), where the columns and rows represent actual gestures and predicated signals, respectively. Each bimanual gesture was repeated 50 times. The success rates are 94%, 92%, 100%, and 100% for the predicted signals of A, B, C, and D, respectively. The overall accuracy is 96.5%. The high-fidelity EMGs recording and high classification accuracy can enable the real-time, high-precision control of a virtual character and a quadcopter using human bimanual gestures. As shown in Figure 2.7.4, the control of a virtual tiger in a 3D game engine is realized using bimanual gestures. Here, A, B, C, and D correspond to "walk forward," "turn left," "turn right," and "jump," respectively.

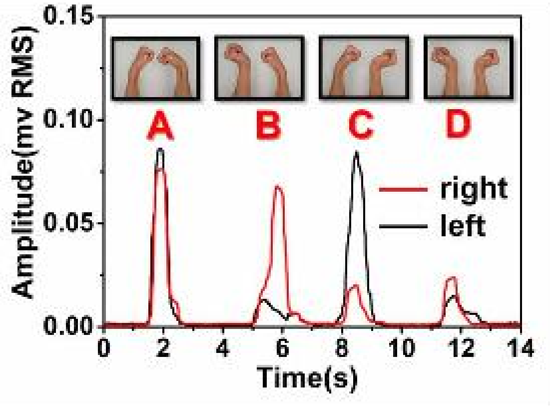

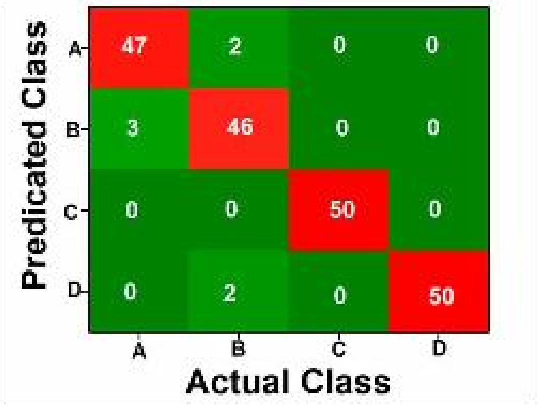

	A	B	C	D
A	47	2	0	0
B	3	46	0	0
C	0	0	50	0
D	0	2	0	50

Figure 2.7.2 EMG signals recorded from the forearms associated with 4 different bimanual gestures (Inset), which can be classified into 4 distinct control signals, termed A, B, C, and D.

Figure 2.7.3 Confusion matrix that indicates the classification accuracy. Each bimanual gesture was repeated 50 times. The columns and rows represent actual gestures (actual class) and predicted signals (predicated class), respectively. Numbers are highlighted in the box to show the distribution of predicted signals in each actual gesture motion.

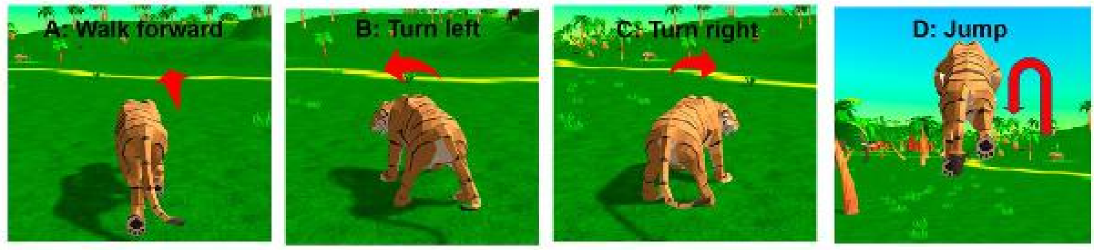

Figure 2.7.4 Control of a virtual tiger in a 3D game engine using bimanual gestures, where A, B, C, and D correspond to “walk forward,” “turn left,” “turn right,” and “jump,” respectively.

The quadcopter used in the research is shown in Figure 2.7.5. Four bimanual gestures are assigned to 5 different quadcopter control commands: A, “fly forward”; B, “turn left”; C, “turn right”; first D, “take off”; and second D, “land.” As demonstrated in Figures 2.7.6 and 2.7.7, the bimanual gestures can precisely control the motion and trajectory of the quadcopter in a real-time and wireless manner.

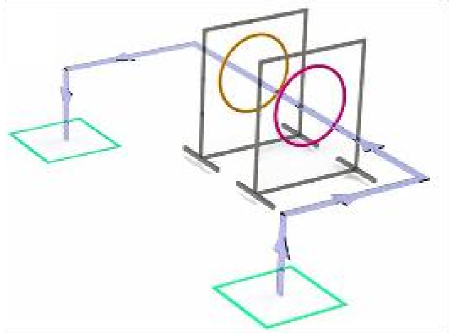

Figure 2.7.5 (left) A photograph of the quadcopter used in the research.

Figure 2.7.6 (right) Schematic illustrations of the quadcopter trajectory controlled by bimanual gestures, where arrows indicate the flying direction.

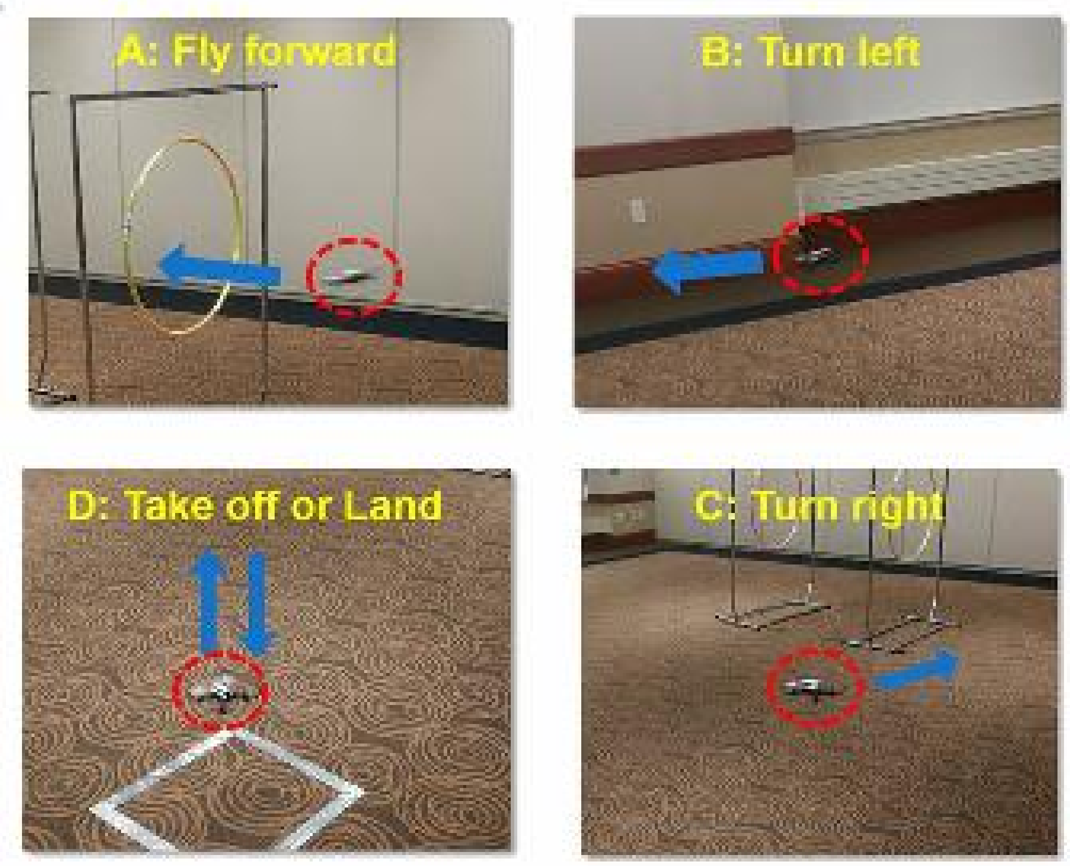

Figure 2.7.7 Images of the quadcopter control by bimanual gestures, where A, B, C, and D correspond to “fly forward,” “turn left,” “turn right,” and “take off or land,” respectively.

2.8 Conclusion

In summary, we report the synthesis of multiscale porous SEBS substrates and their applications in multifunctional on-skin electronics with passive-cooling capabilities. In addition to passive cooling, the enabled on-skin devices exhibit a collection of other compelling features, such as high breathability, waterproofing, and recyclability. On-skin electronics with the unique combination of these desired features have not been achieved yet.

In this part of research, our group members cooperated with each other and I did most of the fabrication works and part of the testing works. I synthesized the SEBS substrates, fabricated the on-skin electronics via spray printing of Ag NWs and participated in all the tests.

We demonstrate the applications of the enabled on-skin devices in 1) high-fidelity monitoring of biopotentials, body temperatures, skin hydration levels, pulse waveforms, and blood pressures; 2) efficient administration of programmed electrical interventions; and 3) high-precision control of a soft robotic hand, a virtual character, and a quadcopter. In addition, the reported fabrication approaches, for both the synthesis of multiscale porous SEBS substrates and printing of bioelectronic devices, are simple, inexpensive, and scalable, which can facilitate the high-throughput manufacturing and practical applications.

Chapter 3

Phase-Separation-Induced Porous Conductive Nanocomposites Composed of Silver Nanowires and Polyurethane

3.1 Introduction

As skin-interfaced electronics require high conductivity and stretchability simultaneously, conductive polymer nanocomposites which usually have excellent performances on mechanical and electrical properties have attracted great attention in recent years (74). However, it is a challenge to achieve a trade-off between conductivity and stretchability because of the molecular mechanisms operating during material deformation. Nanocomposites based on the percolation network of high-aspect-ratio conductive nanomaterials (e.g. tubes and nanowires) in polymer matrices is one of the best-known solutions (37, 79, 80). Using specific alignment can further improve the conductivity (81). Besides, breathability is important for user comfort and minimal inflammation risks (31) and manufacturing cost also should be considered. In addition, skin-interfaced electronics made of polymer nanocomposites with strain-sensitive property (e.g. strain sensors) have been widely reported (71-73). However, the research on polymer nanocomposites with strain-insensitive property is still rare.

In this work, we report the development of strain-insensitive conductive nanocomposite for skin-interfaced electronics. It exhibits not only excellent strain-insensitivity property, but also other desired features, such as low percolation threshold, outstanding breathability, conductivity, strain-insensitivity, mechanical and electrical robustness and durability. The conductive porous silver nanowire/polyurethane nanocomposite is enabled by well-controlled in-situ distribution of conductive nanofiller (i.e., silver nanowires) on the surface of microscale pores. And the judiciously engineered structure enables substantially decreased (~50 times) percolation threshold and excellent strain-insensitivity property. For further application, we plan to apply the Ag NW/PU nanocomposites to bioelectrical devices for stress monitoring and brain interfacing in future works.

3.2 Materials

Polyurethane pellets (Texin® RxT85A) were bought from Covestro. Tetrahydrofuran (THF) and 1-butanol were purchased from Fisher Scientific. Silver nanowires (Ag NW) dispersed in ethanol (Ag NW-40, 20mg/ml) was purchased from ACS Material. All other chemicals used were of analytical grade.

3.3 Synthesis of porous conductive Ag NW/PU nanocomposites

The method used to make Ag NW/PU nanocomposites is still phase separation method, which is simple, inexpensive and scalable. We used THF (boiling point, 66°C) as solvent, and the mixture of 1-butanol (boiling point, 117.7°C) and Ag NWs solution as nonsolvent.

To obtain conductive, stretchable and biocompatible nanocomposites consisting of Ag NWs dispersed in elastomer, we adopt polyurethane as the elastomer. For one reason, it has high stretchability and solution processability. For another reason, the PU elastomer forms strong interfacial interactions with Ag NWs due to the hydrogen bond between poly(vinyl pyrrolidone) (PVP) surfactant on the surface of Ag NWs and urethane groups of PU elastomer, as shown in Figure 3.3.1.

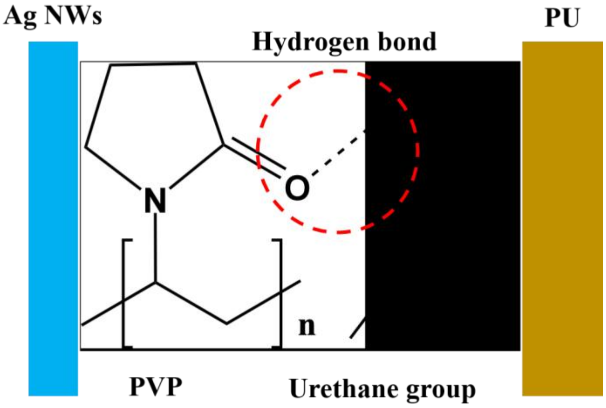

Figure 3.3.1 Schematic illustration of PVP-decorated Ag NWs and PU bonded by Hydrogen bonds.

The phase separation-based process starts with the preparation of a precursor solution of PU and 1-butanol combined with Ag NWs in THF. To prepare the precursor solution, we first dissolve PU powders in THF to obtain PU stock solution (70 mg/ml), which was then mixed with Ag NWs solution and 1-butanol. Specifically, 1 ml of PU stock solution was mixed with various amount of nonsolvent solutions (i.e., 1-butanol and Ag NWs solution). After 10 min of bath sonication of the as-prepared precursor solution (Branson CPX2800H Ultrasonic cleanser, low power mode), the conductive and stretchable nanocomposites were obtained by drop-casting the resulting solution on an aluminum foil and drying at ambient conditions. As shown in Figure 3.3.2, during the drying process, phase separation was triggered by the evaporation of volatile THF in the as-prepared homogeneous solution (Figure 3.3.2, left), where a PU-rich solid phase containing PU and a nonsolvent liquid phase containing Ag NWs (Figure 3.3.2, middle) were formed. Complete evaporation of solvent and nonsolvent results in the formation of Ag NW/PU nanocomposite films with hierarchical pores (Figure 3.3.2, right).

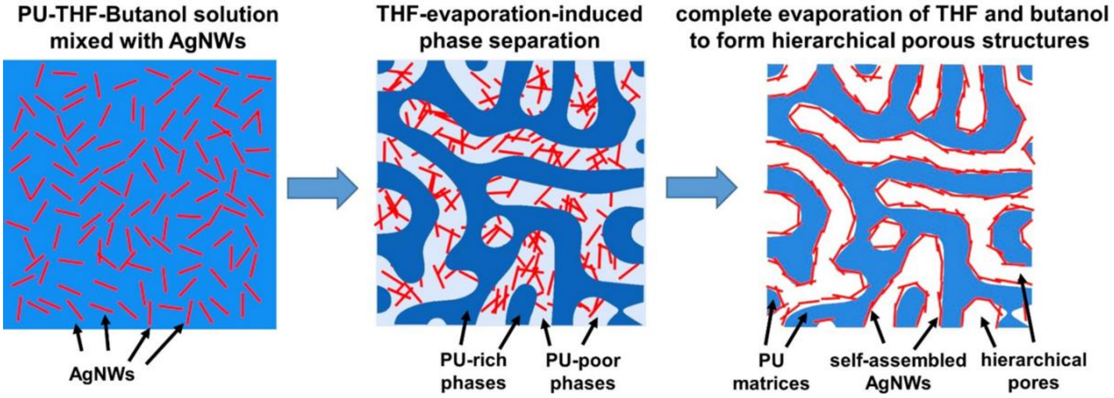

Figure 3.3.2 Schematic showing that the initial solution (left) is separated into a PU-rich phase and a PU-poor phase during dry-casting (middle). Subsequent solvent and nonsolvent evaporation forms the Ag NW/PU nanocomposite with hierarchical pores (right). Red wires, Ag NWs; blue areas, PU.

The porous conductive Ag NW/PU nanocomposites with various Ag NW contents and pore sizes are fabricated by using various amount of Ag NWs, and the volumetric ratios between PU stock solution and nonsolvent in precursor solution. The effects of nonsolvent in the phase separation process and the effect of volume fractions of Ag NWs were systematically investigated as follows.

Effects of amount of nonsolvent

Phase separation has a pronounced effect on conductivity, stretchability and softness of the Ag NW/PU nanocomposites. And a key factor is the amount of nonsolvent we used. As shown in Figure 3.3.3, at a fixed weight ratio of 8:70 for Ag NWs: PU (1ml 70mg/ml PU solution and 0.4ml 20mg/ml Ag NWs solution), when the volume of nonsolvent is 0.4ml, the electrical conductivity of the Ag NW/PU nanocomposite film is very low. As the volume of nonsolvent is increased to 0.5ml, the electrical conductivity is almost 2 orders of magnitude greater than that of 0.4ml. In the range from 0.5ml to 1.1ml, the conductivity values are relatively stable and reach the highest when the volume of nonsolvent is 0.8ml. It shows integrity failure when the volume of nonsolvent is increased up to 1.3ml.

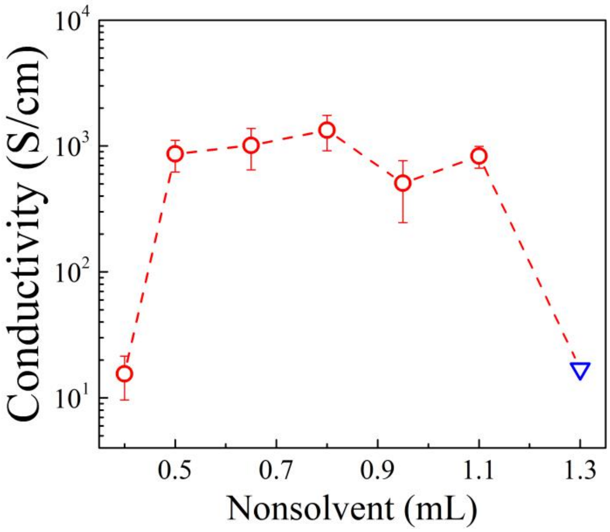

Figure 3.3.3 Electrical conductivity of the Ag NW/PU nanocomposites change with volume of nonsolvent used in the synthesis process.

Figure 3.3.4 shows curves of the relative resistance change with applied strain of Ag NW/PU nanocomposite films using different volumes of nonsolvent. The relative resistance change of the film using 0.95ml nonsolvent increases rapidly while relative resistance changes of films using 0.4ml and 0.65ml nonsolvent respectively increases very slowly. It indicates the more nonsolvent we use, the worse the strain-insensitivity will be at the fixed ratio for Ag NWs and PU. For the Ag NW/PU nanocomposite film using 0.8ml nonsolvent, the resistance change slowly when the strain is in the range of 100%, which is usually enough for on-skin electronics.

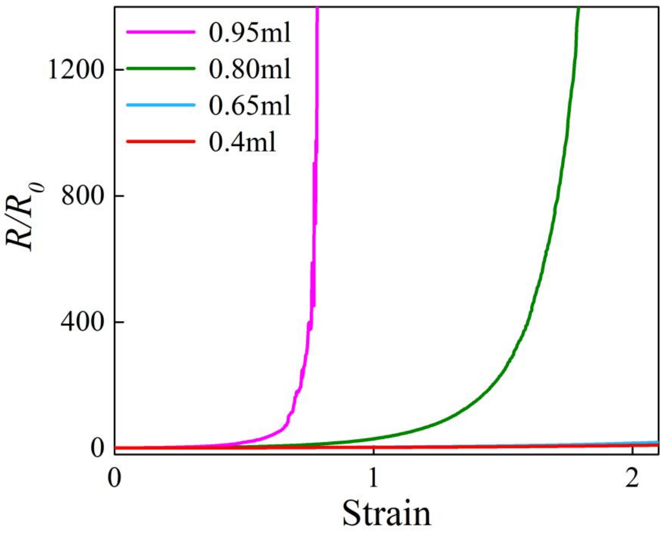

Figure 3.3.4 Relative resistance change measurement under various strains for Ag NW/PU nanocomposite films using different volumes of nonsolvent.

Figure 3.3.5 shows the modulus and stretchability of Ag NW/PU nanocomposite films change with the amount of nonsolvent used. At a fixed weight ratio of 8:70 for Ag NWs and PU , 0ml (which makes the film nonporous), 0.4ml, 0.65ml, 0.8ml, 0.95ml of nonsolvent were added respectively. The modulus and stretchability decrease simultaneously.

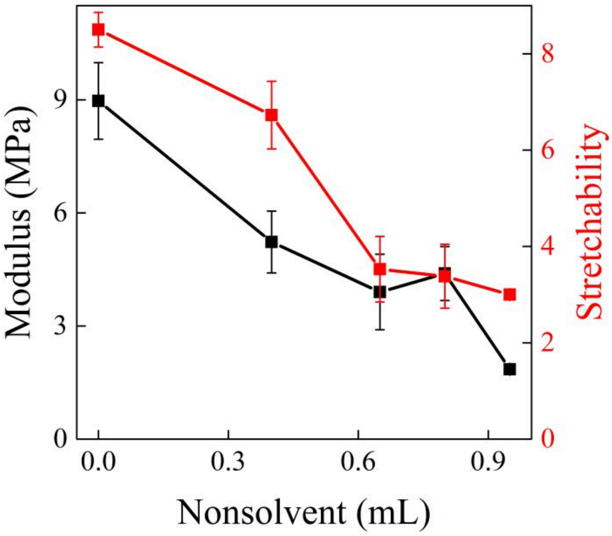

Figure 3.3.5 Changes of modulus (black) and stretchability (red) of the Ag/PU nanocomposite films according to the volume of nonsolvent.

To sum up, the optimum composition to maintain high conductivity and stretchability simultaneously is 0.8:1 volume ratio for nonsolvent and 7% PU solution. The amount of Ag NW can be adjusted as needed.

Effects of amount of Ag NWs

The most important factor that affects the conductivity of the Ag/PU nanocomposite is the amount of Ag NWs. At a fixed volume ratio of 0.8:1 for nonsolvent and 7% PU solution, 0.3ml, 0.4ml, 0.8ml of Ag NWs were added respectively when preparing precursor solutions. As shown in Figure 3.3.6, when the volume fraction of Ag NW is small, the resistance of the film increases very fast even within the strain range of 100%. When the volume fraction of Ag NW increased up to 0.0038%, the resistance of the film increases slowly, indicating good strain-insensitivity.

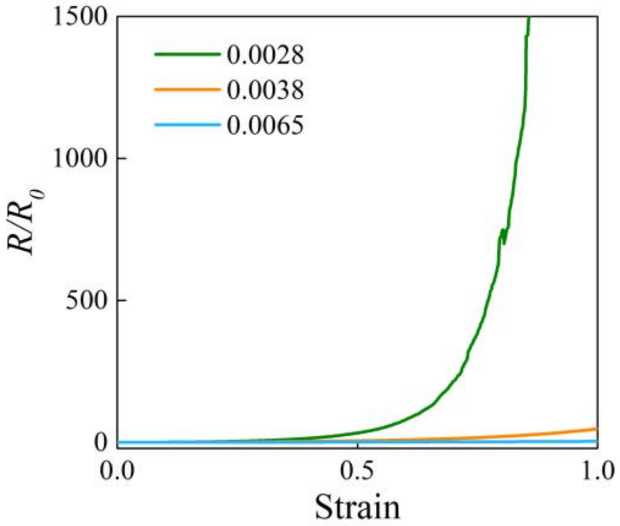

Figure 3.3.6 Relative resistance change measurement under various strains for Ag NW/PU nanocomposite films with different volume fractions of Ag NWs.

Summary

In this part, we talk about the phase separation-induced synthesis of porous Ag NW/PU nanocomposites, and analyzed the key factors that can affect the conductivity and stretchability of the nanocomposite films in the fabrication process. To sum up, we mix PU stock solution (70 mg/ml in THF) with Ag NWs solution and 1-butanol to prepare the precursor solution. The optimized composition is 1:0.8 volume ratio for PU solution and nonsolvent, and for Ag NWs solution, we can adjust the amount as needed.

3.4 Characterizations of porous conductive Ag NW/PU nanocomposites

The percolation threshold of the Ag NW/PU nanocomposite is very low because of the high aspect ratio of the Ag NWs we use. In this work, we refer to an improved interparticle distance (IPD) model with two descriptive dispersion parameters (61). As the length(l) of Ag NW we use is 20~30 μm , $l \gg$ IPD. Here, IPD = 10 nm was taken as the criterion for the calculation of percolation thresholds. In a nonporous composite, assume Ag NWs are perfectly dispersed in the nanocomposite, we can use the following equation to calculate the percolation threshold (V_c)

$$V_c = \frac{27\pi d^2}{4l^2}$$

where l and d denotes the length and diameter of the filler (Ag NWs).

However, this equation is not applicable for our porous composite as the distribution of Ag NWs are guided by the phase separation process, which allows their uniform distribution in the porous walls. Considering various pore sizes of Ag

NW/PU nanocomposites using different volume of nonsolvent while fabricating, we modify the equation and get

$$V_c = \frac{\frac{1}{4} S n_c \pi d^2 l}{V}$$

where n_c represents critical density, which means the number of fillers per unit area, and S is the surface area. Here, $n_c * l^2 = 5.63726$, d=40 nm, l =30 μm, $S=f(D_P)$ where D_P denotes pore diameter.

With all the known values, we can get the plot of percolation threshold V_c as a function of pore size, as shown in Figure 3.4.1.

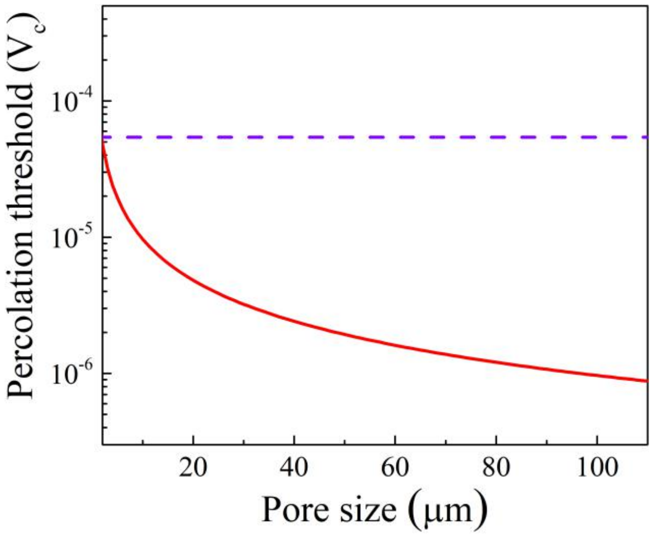

Figure 3.4.1 Percolation threshold of Ag NW/PU nanocomposites with different pore sizes.

As shown in Figure 3.4.2, the SEM images of Ag NW/PU nanocomposites using 0.65ml, 0.8ml, 0.95ml of nonsolvent show that the Ag NWs are interconnected in hierarchical pores. The number-weighed mean pore sizes are 16.8μm for nanocomposites using 0.65ml of nonsolvent,10.3μm for nanocomposites using 0.8ml of nonsolvent and 4.3μm for nanocomposites using 0.95ml of nonsolvent. From the second equation, the percolation of the nanocomposites is calculated to be as low as 0.00062.

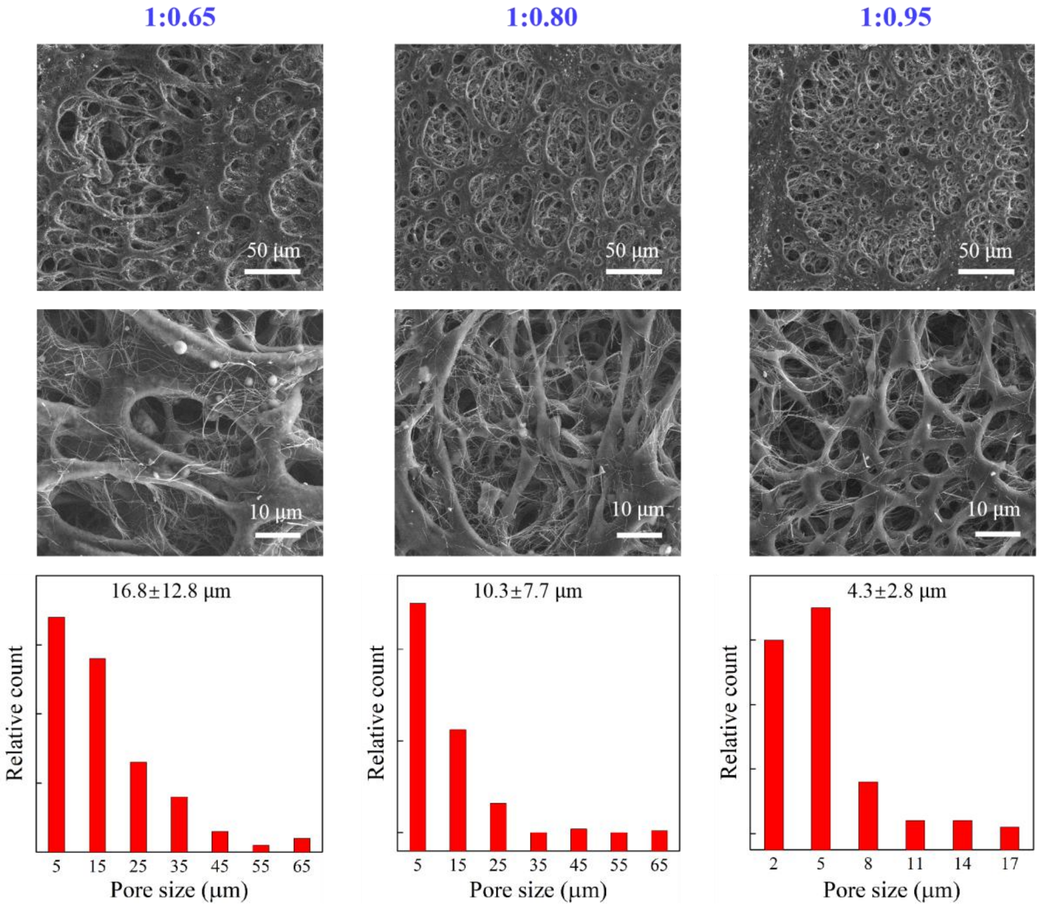

Figure 3.4.2 SEM images of Ag NW/PU nanocomposites using 0.65ml, 0.8ml, 0.95ml of nonsolvent and the pore size distributions.

The low percolation threshold of Ag NWs results in high conductivity of the nanocomposites. Figure 3.4.3 shows the conductivity of the Ag NW/PU nanocomposites change with the volume fraction of Ag NWs. We conduct three series of experiments using different volume of nonsolvent. It demonstrates that the porous nanocomposites show higher conductivity than the nonporous nanocomposite. And for the porous nanocomposites, the one using 0.8ml nonsolvent perform better than the one using 1.1ml nonsolvent. The maximum conductivity is 2038 S/cm at the volume ratio of 0.8:1 for nonsolvent and PU stock solution and weight ratio of 16:70 for Ag NWs and PU.

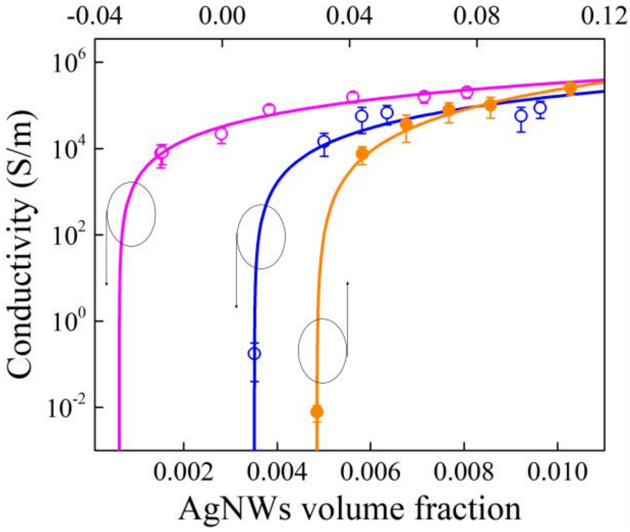

Figure 3.4.3 Electrical conductivity of Ag NW/PU nanocomposites with various Ag NWs fraction. The three curves correspond to porous nanocomposites using 0.8ml nonsolvent (purple) and 1.1ml nonsolvent (blue) respectively, and nonporous nanocomposite (orange).

In addition to the high conductivity, the Ag NW/PU nanocomposite also exhibits a number of other desired features including high stretchability, high breathability, low elastic modulus and thermal stability. First, the stretchability of the nanocomposite can be up to 750% as shown in Figure 3.3.5. Second, as shown in Figure 3.4.4, the porous Ag NW/PU nanocomposite film shows a high water vapor transmission rate (0.02 $g \cdot cm^{-2} \cdot h^{-1}$) due to the interconnected hierarchical pores, which is about 7 times of that of nonporous films with same thickness and is close to the porous SEBS substrate discussed in chapter 2. The high WVTR can minimize inflammatory reactions caused by sweat accumulation.

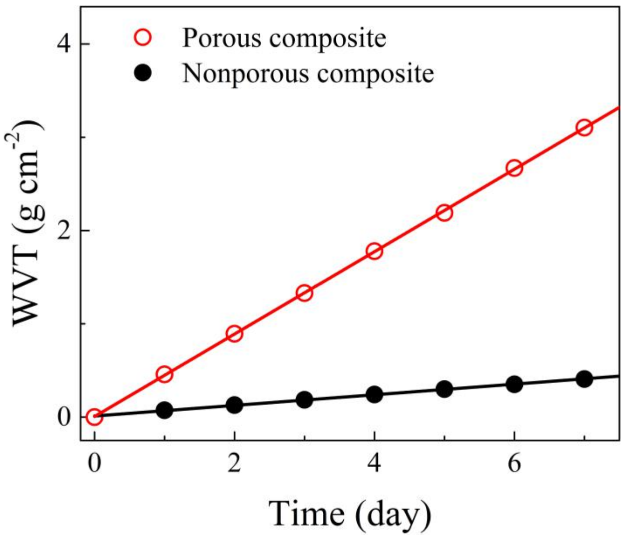

Figure 3.4.4 Water vapor transmission rates(WVTR) of porous Ag NW/PU nanocomposite (red) and nonporous Ag NW/PU nanocomposite (black) as a function of elapsed time.

The Ag NW/PU nanocomposites are relatively thermally stable. Considering the melt temperature of PU is around 190℃, the heating temperature is set to be 80 ℃, 100 ℃, 130 ℃. Here, the nanocomposite films are fabricated still at room temperature, and then heated for half an hour under 80 ℃, 100 ℃, 130 ℃ respectively. As shown in Figure 3.4.5, Young's modulus of porous Ag/PU nanocomposite films increase with the temperature. The modulus of the nanocomposite film without thermal heating is 1.2 MPa, but even when the film is heated at 130 ℃ for 30 minutes, the modulus is still not very large (~4 MPa). As a comparison, the modulus of nonporous PU is ~9 MPa.

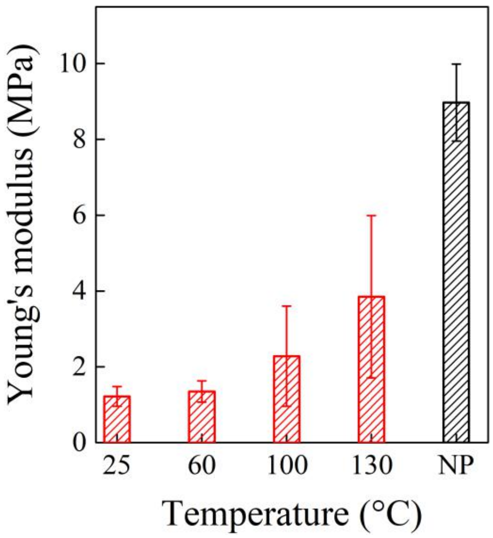

Figure 3.4.5 Young's modulus of porous Ag/PU nanocomposite films processed under different temperatures - room temperature, 80 ℃, 100 ℃, 130 ℃ and 150℃.

As shown in Figures 3.4.6, 3.4.7, the films remain highly conductive and ultrasoft after heating under 80 ℃, 100 ℃, 130 ℃ for half an hour. And Figure 3.4.8 shows that the relative resistances of the heated films increase rapidly when stretched more than 200%, but they can keep strain-insensitivity within 200% stretch, which is enough for on-skin devices.

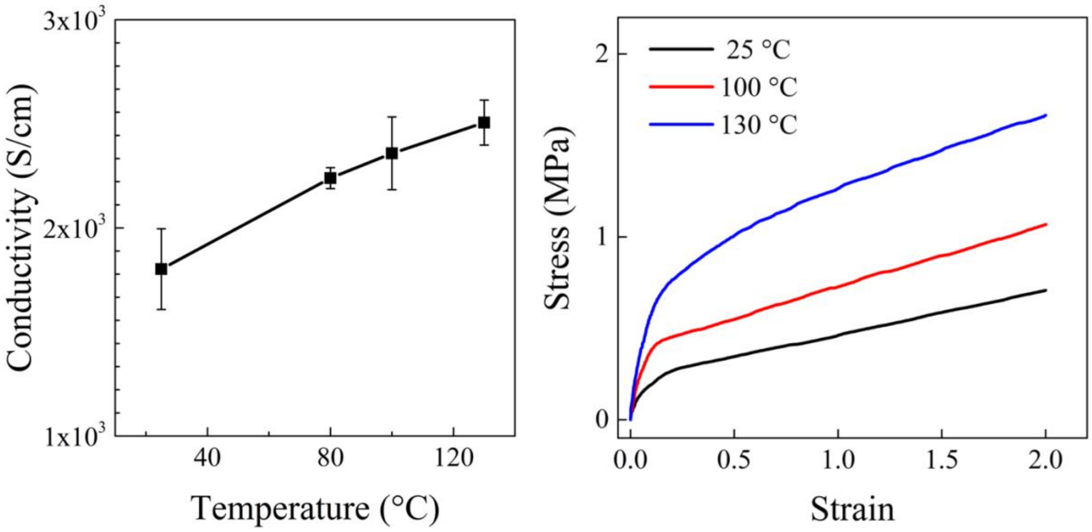

Figure 3.4.6 (left) Conductivity of porous Ag NW/PU nanocomposite films processed under different temperatures - room temperature, 80 ℃, 100 ℃ and 130 ℃.

Figure 3.4.7 (right) Strain-stress curves of porous Ag NW/PU nanocomposite films processed under different temperatures - room temperature, 80 ℃, 100 ℃ and 130 ℃.

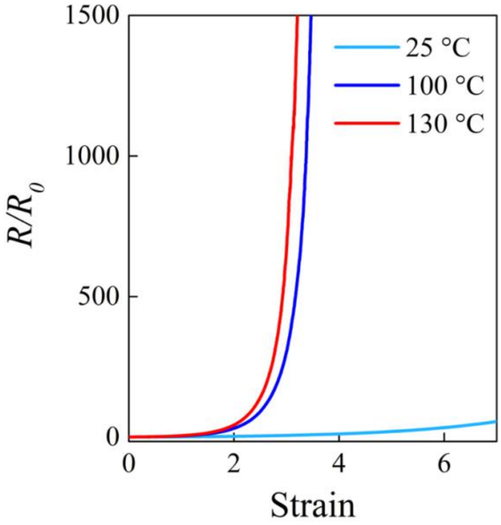

Figure 3.4.8 Relative resistance change with applied strain of porous Ag NW/PU nanocomposite films processed under different temperatures - room temperature, 80 ℃, 100 ℃ and 130 ℃.

Also, the interconnected Ag NWs endow the porous Ag NW/PU nanocomposite with outstanding electromechanical properties. The SEM images under stretching 50% and 100% indicate that the Ag NWs keeps interconnected under stretching, as shown in Figure 3.4.9.

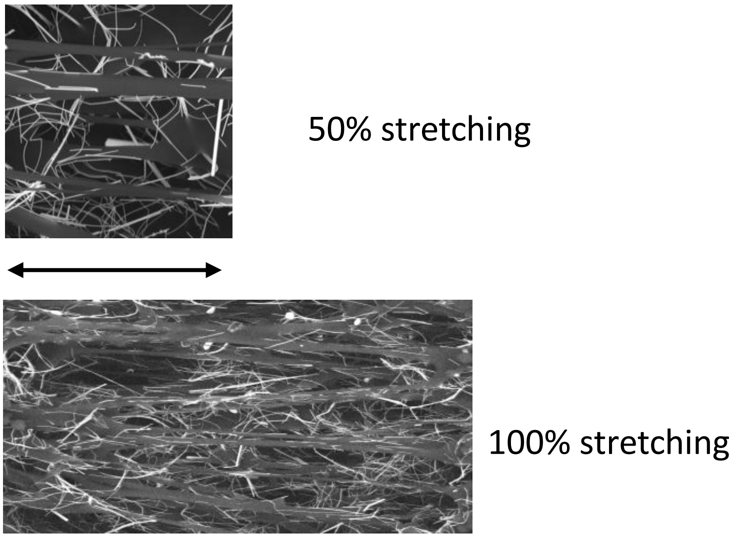

Figure 3.4.9 SEM images under stretching (50%, 100%)

As shown in Figures 3.4.10 and 3.4.11, stretching and washing produce small effects on their electrical properties.

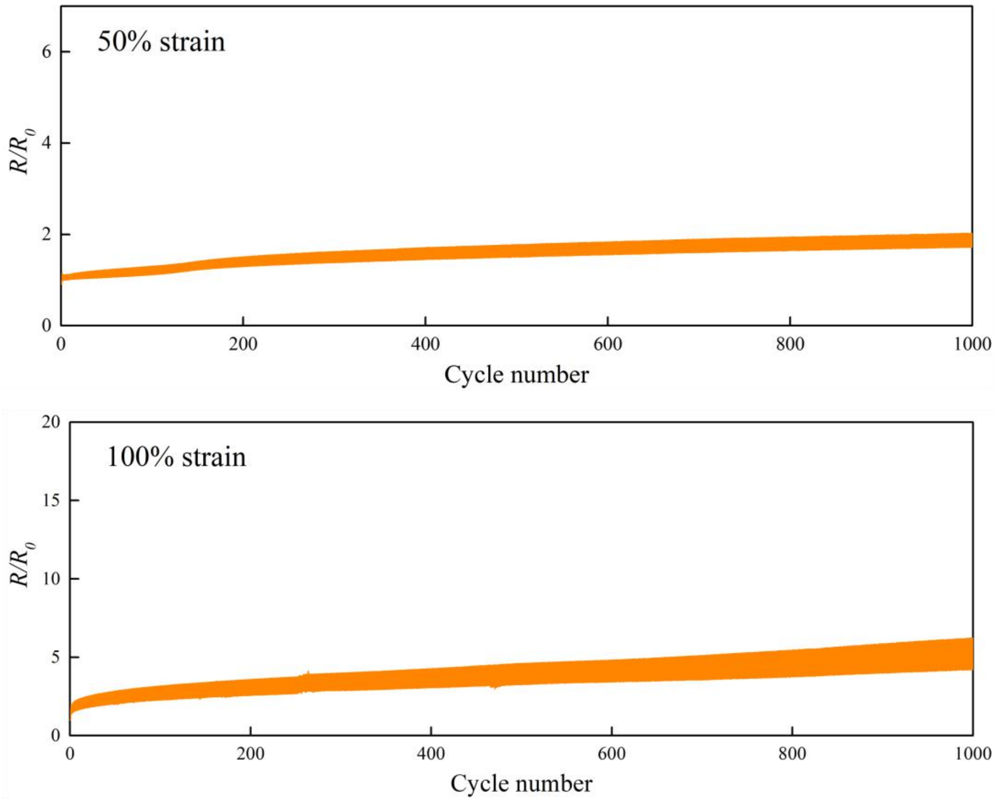

Figure 3.4.10 Normalized electrical resistance changes under the cycling stretching tests. 1,000 cycles of stretching test under the uniaxial strain of 50% and 100%.

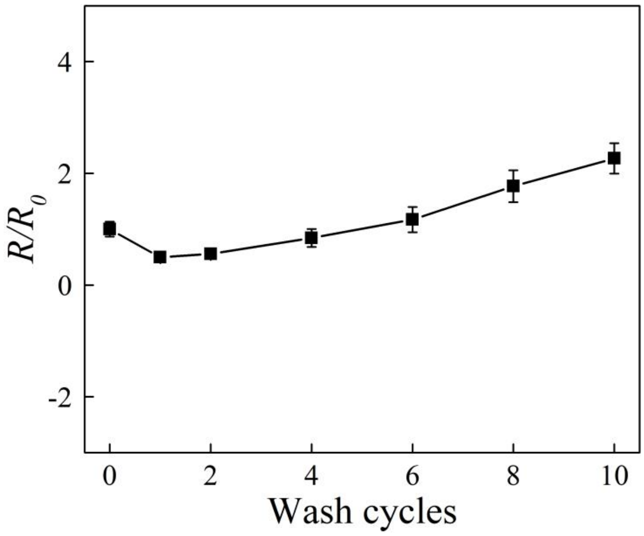

Figure 3.4.11 Normalized electrical resistance changes under the cycling washing tests. 10 cycles of washing for 30 minutes each time.

Furthermore, we also conduct some experiments including knife puncture, hammer impact, twisting and bending to demonstrate the robustness of these films. As shown in Figures 3.4.12 and 3.4.13 , the resistance of the film keeps almost unchanged, which means knife puncture, hammer impact, twisting and bending produce small effects on their electrical properties as well.

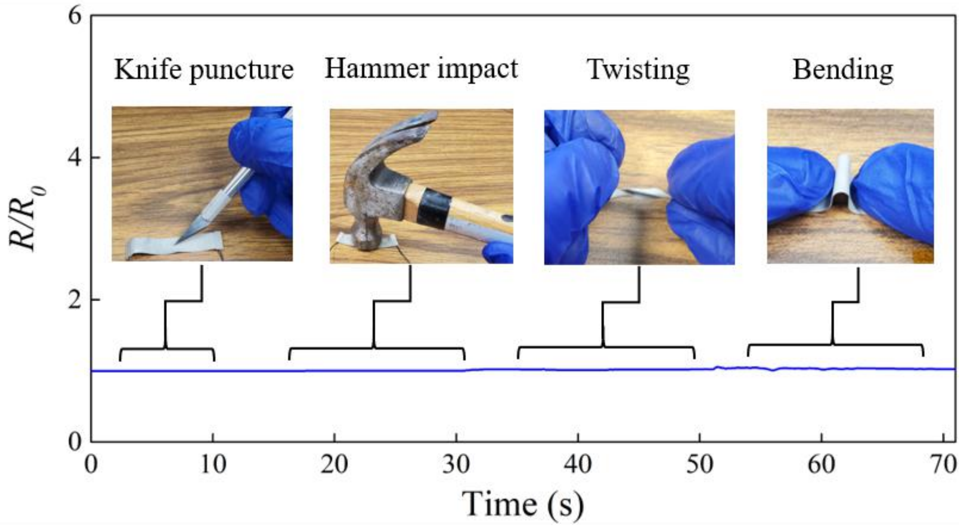

Figure 3.4.12 Normalized electrical resistance changes with time under knife puncture, hammer impact, twisting and bending.

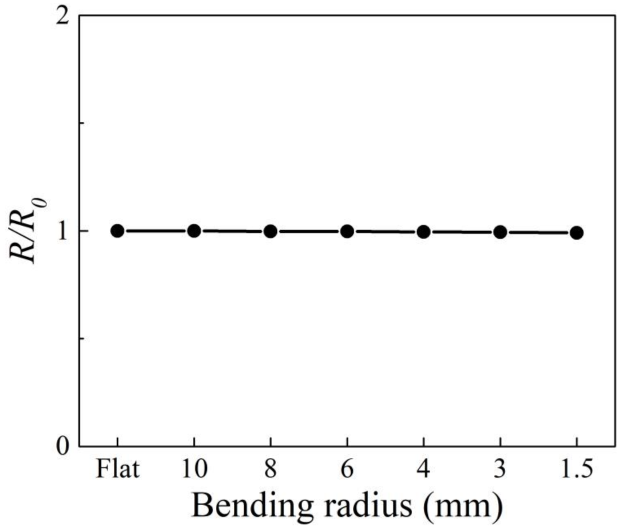

Figure 3.4.13 Normalized electrical resistance changes under bending with different bending radius.

Besides, the electrical conductivity of the porous Ag NW/PU nanocomposite can recover after stretched and be used again. As shown in Figures 3.4.14, the electrical conductivity of the porous conductive Ag/PU nanocomposite becomes low after stretching. Here, we introduce the simple ethanol-assisted method to help the stretched film recovery. Simply wet the used film with ethanol and then wait for it to dry at room temperature. Then the electrical conductivity of that porous nanocomposite film can increase back close to the initial value. For the nonporous nanocomposite films, the conductivity can also recovery to some extent, but the effect is not as good as that of the porous ones.

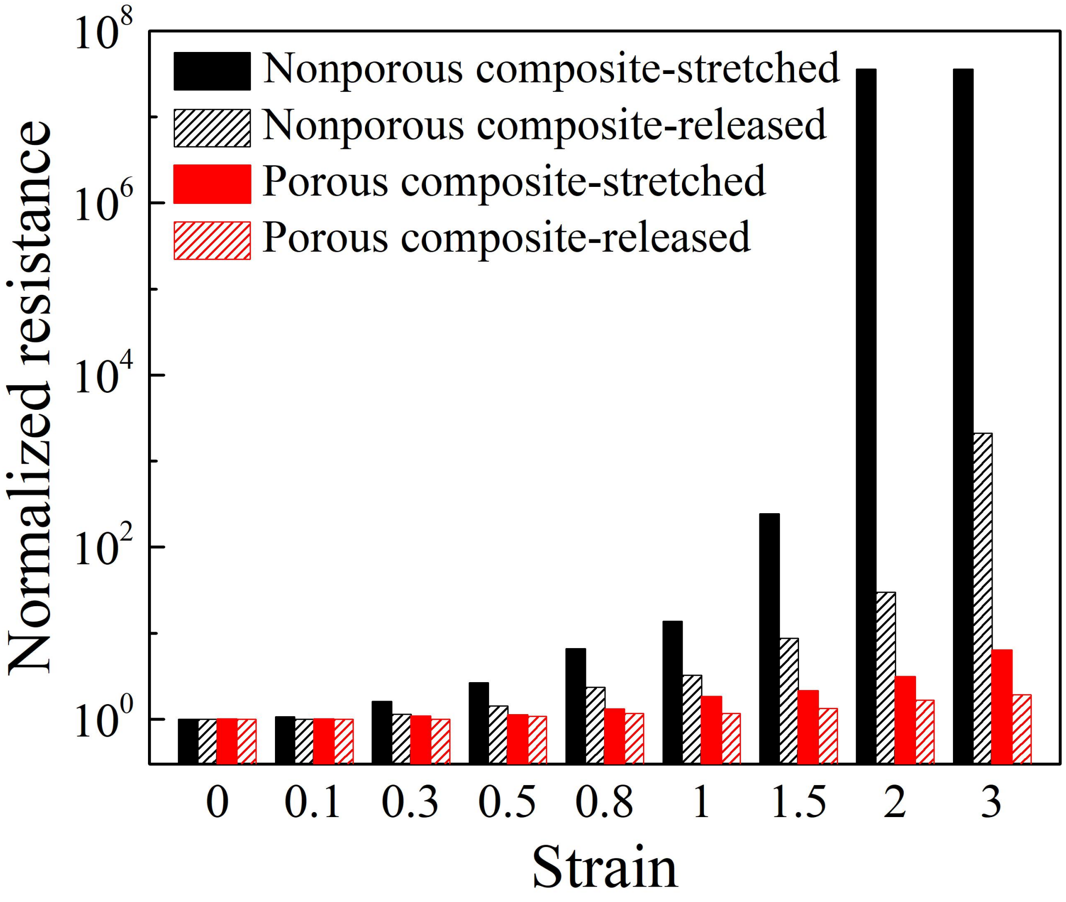

Figure 3.4.14 Comparisons of the resistances of stretched and released nonporous composites and stretched and released porous composites. The released composites have been processed with ethanol for recovery.

3.5 Conclusion

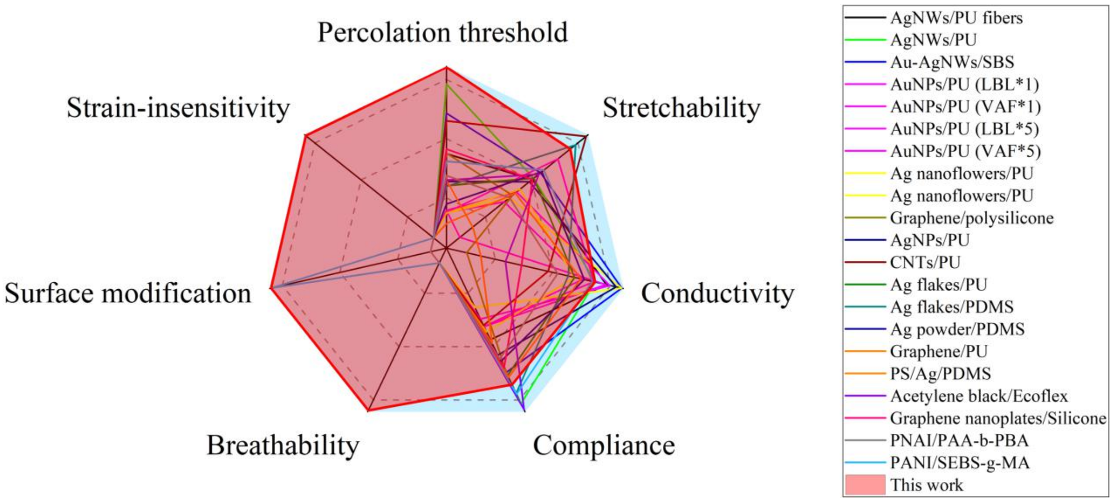

Figure 3.5.1 Comparison of performances of several functional materials, which are recently reported in literatures, in terms of percolation threshold, stretchability, conductivity, compliance, breathability, surface modification and strain-insensitivity. References: 37,62-77.

This part of research focus on the synthesis and characterization of the porous conductive Ag NW/PU nanocomposites.

In this work, we choose phase separation method which is simple, inexpensive and scalable to synthesis the electrically conductive polymer nanocomposites incorporated with conductive nanofillers (i.e. silver nanowires). The Ag NW/PU nanocomposites therefore form hierarchical porous structure. The Ag NWs are well-controlled in-situ distributed on the surface of microscale pores which enables the Ag NW/PU nanocomposites highly conductive. The Ag NW/PU nanocomposites synthesized by phase separation method have a percolation threshold of 0.00062 and can maximum electrical conductivity of 2038 S/cm. In addition to highly conductive, the Ag NW/PU nanocomposites shows other compelling features, such as breathability, strain-insensitivity, mechanical and electrical robustness and durability. As shown in Figure 3.5.1, nanocomposites combined with all these desired features have not been achieved yet. It is expected that the conductive polymer nanocomposites incorporated with well-dispersed Ag NWs will be a promising material for skin-interfaced electronics.

Chapter 4 Conclusions

This thesis explored the multifunctional porous polymer materials for skin-interfaced electronic devices.

In the first part (chapter 2), we first investigated into the reported materials and fabrication methods for skin-interfaced electronics, and adopted SEBS mainly because of its high stretchability and solution processability. We revealed how the interconnected, hierarchical pores of the multifunctional porous SEBS substrates are formed by the phase separation-controlled method. The method is simple, inexpensive and scalable, making it possible for the high-throughput manufacturing in the future. We found that the multifunctional SEBS substrates have outstanding passive-cooling capabilities and high breathability, stemming from the structural engineering of interconnected multiscale porous structure in elastomer. It is also proved to be waterproof and recyclable, as demonstrated by the on-body device testing.

In order to minimize inflammation risks induced by continuous and long-term use of skin-interfaced electronics, we sprayed printing of Ag NWs on prestretched multiscale porous SEBS substrates to preserve the breathability and conductivity while stretching. And finally, we fabricated a variety of prototypic on-skin electronic devices via spray printing and demonstrated some applications of the enabled on-skin devices for continuously monitoring of human vital signals and human-machine interactions.

In the second part (chapter 3), we also investigated the materials and fabrication methods for conductive polymer nanocomposites. For the similar reasons, we chose phase separation method because the method is simple, inexpensive and scalable, and it can form hierarchical porous structure. PU and Ag NWs were chosen as the matrix polymer and conductive nanofillers. We explored how the amount of nonsolvent affect the synthesis process and obtained the optimal volume ratio of 0.8:1 for nonsolvent and 7% PU stock solution. We also found that the content of Ag NWs can be adjusted based on demand. Notably, the judiciously engineered structure enables substantially decreased (~50 times) percolation threshold and excellent strain-insensitivity property. The reduction of percolation threshold can largely reduce the usage of Ag NWs compared to the nonporous Ag NW/PU nanocomposites with comparable conductivity. The porous Ag NW/PU nanocomposites synthesized by phase separation method can achieve a low percolation threshold of 0.00062 and a maximum electrical conductivity of 2038 S/cm. We also demonstrated the thermal stability of the porous Ag NW/PU nanocomposites. Besides, it exhibits other compelling features, such as high breathability, mechanical and electrical robustness and durability.

In terms of the multiscale porous SEBS supporting substrates and the Ag NW/PU nanocomposite as well as other polymer materials or nanocomposites, many research areas are still unexplored. For example, the application of these skin-interfaces electronics for continuous and long-term monitoring human vital signals such as GSR signals has not been explored in this thesis.

References

1. D.-H. Kim et al., Epidermal electronics. Science 333, 838-843 (2011).

2. T. R. Ray et al., Bio-integrated wearable systems: A comprehensive review. Chem. Rev. 119, 5461-5533 (2019).

3. T. Someya, M. Amagai, Toward a new generation of smart skins. Nat. Biotechnol. 37, 382-388 (2019).

4. A. Chortos, J. Liu, Z. Bao, Pursuing prosthetic electronic skin. Nat. Mater. 15, 937-950 (2016).

5. T. Someya, Z. Bao, G. G. Malliaras, The rise of plastic bioelectronics. Nature 540, 379-385 (2016).

6. W. Gao, H. Ota, D. Kiriya, K. Takei, A. Javey, Flexible electronics toward wearable sensing. Acc. Chem. Res. 52, 523-533 (2019).

7. K. Sim, Z. Rao, F. Ershad, C. Yu, Rubbery electronics fully made of stretchable elastomeric electronic materials. Adv. Mater., 10.1002/adma.201902417 (2019).

8. C. Choi, Y. Lee, K. W. Cho, J. H. Koo, D.-H. Kim, Wearable and implantable soft bioelectronics using two-dimensional materials. Acc. Chem. Res. 52, 73-81 (2019).

9. E. J. Markvicka, M. D. Bartlett, X. Huang, C. Majidi, An autonomously electrically selfhealing liquid metal-elastomer composite for robust soft-matter robotics and electronics. Nat. Mater. 17, 618-624 (2018).

10. G. S. C. Bermúdez, H. Fuchs, L. Bischoff, J. Fassbender, D. Makarov, Electronic-skin compasses for geomagnetic field-driven artificial magnetoreception and interactive electronics. Nat. Electron. 1, 589-595 (2018).

11. B. Yin, X. Liu, H. Gao, T. Fu, J. Yao, Bioinspired and bristled microparticles for ultrasensitive pressure and strain sensors. Nat. Commun. 9, 5161 (2018).

12. S. Hong et al., Wearable thermoelectrics for personalized thermoregulation. Sci. Adv. 5, eaaw0536 (2019).

13. K. Sim et al., Three-dimensional curvy electronics created using conformal additive stamp printing. Nat. Electron., 2, 471-479 (2019).

14. K. Sim et al., Metal oxide semiconductor nanomembrane-based soft unnoticeable multifunctional electronics for wearable human-machine interfaces. Sci. Adv. 5, eaav9653 (2019).

15. S. Yang et al., “Cut-and-paste” manufacture of multiparametric epidermal sensor systems. Adv. Mater. 27, 6423-6430 (2015).

16. S. Kabiri Ameri et al., Graphene electronic tattoo sensors. ACS Nano 11, 7634-7641 (2017).

17. Z. Xue, H. Song, J. A. Rogers, Y. Zhang, Y. Huang, Mechanically‐guided structural designs in stretchable inorganic electronics. Adv. Mater. 10.1002/adma.201902254 (2019).

18. G. Chen et al., Plasticizing silk protein for on‐skin stretchable electrodes. Adv. Mater. 30, e1800129 (2018).

19. J. Y. Oh et al., Intrinsically stretchable and healable semiconducting polymer for organic transistors. Nature 539, 411-415 (2016).

20. S. Wang et al., Skin electronics from scalable fabrication of an intrinsically stretchable transistor array. Nature 555, 83-88 (2018).

21. H.-J. Kim, K. Sim, A. Thukral, C. Yu, Rubbery electronics and sensors from intrinsically stretchable elastomeric composites of semiconductors and conductors. Sci. Adv. 3, e1701114 (2017).

22. X. Cheng, Y. Zhang, Micro/nanoscale 3D assembly by rolling, folding, curving, and buckling approaches. Adv. Mater. 31, e1901895 (2019).

23. D. Son et al., An integrated self-healable electronic skin system fabricated via dynamic reconstruction of a nanostructured conducting network. Nat. Nanotechnol. 13, 1057-1065 (2018).

24. B. C. Tee, C. Wang, R. Allen, Z. Bao, An electrically and mechanically self-healing composite with pressure- and flexion-sensitive properties for electronic skin applications. Nat. Nanotechnol. 7, 825-832 (2012).

25. C. M. Boutry et al., A sensitive and biodegradable pressure sensor array for cardiovascular monitoring. Adv. Mater. 27, 6954-6961 (2015).

26. T. Lei et al., Biocompatible and totally disintegrable semiconducting polymer for ultrathin and ultralightweight transient electronics. Proc. Natl. Acad. Sci. U.S.A. 114, 5107-5112 (2017).

27. W. Gao et al., Fully integrated wearable sensor arrays for multiplexed in situ perspiration analysis. Nature 529, 509-514 (2016).

28. M. Bariya, H. Y. Y. Nyein, A. Javey, Wearable sweat sensors. Nat. Electron. 1, 160-171(2018).

29. T. Wang et al., Tactile chemomechanical transduction based on an elastic microstructured array to enhance the sensitivity of portable biosensors. Adv. Mater. 31,

e1803883 (2019).

30. Z. Jiang et al., Highly stretchable metallic nanowire networks reinforced by the underlying randomly distributed elastic polymer nanofibers via interfacial adhesion improvement. Adv. Mater. 31, e1903446 (2019).

31. A. Miyamoto et al., Inflammation-free, gas-permeable, lightweight, stretchable on skin electronics with nanomeshes. Nat. Nanotechnol. 12, 907-913 (2017).

32. H. Jin et al., Highly durable nanofiber-reinforced elastic conductors for skin-tight electronic textiles. ACS Nano 13, 7905-7912 (2019).

33. B. Sun et al., Gas‐permeable, multifunctional on‐skin electronics based on laser‐induced porous graphene and sugar‐templated elastomer sponges. Adv. Mater. 30, e1804327 (2018).

34. J.T. Reeder et al., Waterproof, electronics-enabled, epidermal microfluidic devices for sweat collection, biomarker analysis, and thermography in aquatic settings. Sci. Adv. 5, eaau6356 (2019).

35. Z. Zou et al., Rehealable, fully recyclable, and malleable electronic skin enabled by dynamic covalent thermoset nanocomposite. Sci. Adv. 4, eaaq0508 (2018).

36. S. Choi et al., Stretchable heater using ligand-exchanged silver nanowire nanocomposite for wearable articular thermotherapy. ACS Nano 9, 6626-6633 (2015).

37. S. Choi et al., Highly conductive, stretchable and biocompatible Ag-Au core-sheath nanowire composite for wearable and implantable bioelectronics. Nat. Nanotechnol. 13, 1048-1056 (2018).

38. A. Hazarika et al., Woven Kevlar fiber/polydimethylsiloxane/reduced graphene

oxide composite-based personal thermal management with freestanding Cu-Ni core-shell nanowires. Nano Lett. 18, 6731-6739 (2018).

39. J. Mandal et al., Hierarchically porous polymer coatings for highly efficient passive daytime radiative cooling. Science 362, 315-319 (2018).

40. P.-C. Hsu et al., Radiative human body cooling by nanoporous polyethylene textile. Science 353, 1019-1023 (2016).

41. T. Li et al., A radiative cooling structural material. Science 364, 760-763 (2019).

42. R. Wang et al., Torsional refrigeration by twisted, coiled, and supercoiled fibers. Science 366, 216-221 (2019).

43. F. Wang et al., Progress report on phase separation in polymer solutions. Adv. Mater. 31, e1806733 (2019).

44. Y. Peng et al., Nanoporous polyethylene microfibres for large-scale radiative cooling fabric. Nat. Sustain. 1, 105-112 (2018).

45. N. Matsuhisa et al., Printable elastic conductors by in situ formation of silver nanoparticles from silver flakes. Nat. Mater. 16, 834-840 (2017).

46. Kelly et al., All-printed thin-film transistors from networks of liquid-exfoliated nanosheets. Science 356, 69-73 (2017).

47. P. C. Hsu et al., Personal thermal management by metallic nanowire-coated textile. Nano Lett. 15, 365-371 (2015).

48. N. N. Shi et al., Thermal physiology. Keeping cool: Enhanced optical reflection and radiative heat dissipation in Saharan silver ants. Science 349, 298-301 (2015).

49. H.U. Chung et al., Binodal, wireless epidermal electronic systems with in-sensor

analytics for neonatal intensive care. Science 363, eaau0780 (2019).

50. P. Sarzi-Puttini et al., Seminars in Arthritis and Rheumatism (Elsevier, 2005), vol. 35, pp. 1-10.

51. B. Xu et al., An epidermal stimulation and sensing platform for sensorimotor prosthetic control, management of lower back exertion, and electrical muscle activation. Adv. Mater. 28, 4462-4471 (2016).

52. Y. Ma et al., Relation between blood pressure and pulse wave velocity for human arteries. Proc. Natl. Acad. Sci. U.S.A. 115, 11144-11149 (2018).

53. N. Luo et al., Flexible piezoresistive sensor patch enabling ultralow power cuffless blood pressure measurement. Adv. Funct. Mater. 26, 1178-1187 (2016).

54. K. Meng et al., Flexible weaving constructed self‐powered pressure sensor enabling continuous diagnosis of cardiovascular disease and measurement of cuffless blood pressure. Adv. Funct. Mater. 29, 1806388 (2019).

55. J. Lin et al., Laser-induced porous graphene films from commercial polymers. Nat. Commun. 5, 5714 (2014).

56. C. Poon, Y. Zhang, “Cuff-less and noninvasive measurements of arterial blood pressure by pulse transit time” in 2005 IEEE Engineering in Medicine and Biology 27th Annual Conference (IEEE, 2006), pp. 5877-5880.

57. Chen, Y., Lu, B., et al. Breathable and Stretchable Temperature Sensors Inspired by Skin. Sci Rep 5, 11505 (2015).

58. Lee, S. , et al. Ultrasoft electronics to monitor dynamically pulsing cardiomyocytes. Nature Nanotechnology (2019).

59. You Jun Fan, Xin Li, et al. Highly Robust, Transparent, and Breathable Epidermal Electrode. ACS Nano 12 (9), 9326-9332 (2018).

60. Yang W， Li N W， Zhao S，et al. A Breathable and Screen‐Printed Pressure Sensor Based on Nanofiber Membranes for Electronic Skins[J]. Advanced Materials Technologies, 1700241 (2017).

61. Li, J. et al., Correlations between percolation threshold, dispersion state, and aspect ratio of carbon nanotubes. Adv. Funct. Mater. 17, 3207-3215 (2007).

62. Lu, Y.;Jiang, J.;Yoon, S.;Kim, K.-S.;Kim, J.-H.;Park, S.;Kim, S.-H.; Piao, L. High-performance stretchable conductive composite fibers from surface-modified silver nanowires and thermoplastic polyurethane by wet spinning. ACS applied materials & interfaces, 10, 2093-2104 (2018).

63. Zhu, H.-W.;Gao, H.-L.;Zhao, H.-Y.;Ge, J.;Hu, B.-C.;Huang, J.; Yu, S.-H. Printable elastic silver nanowire-based conductor for washable electronic textiles. Nano Research, 13, 2879-2884 (2020).

64. Kim, Y.;Zhu, J.;Yeom, B.;Di Prima, M.;Su, X.;Kim, J. G.;Yoo, S. J.;Uher, C.; Kotov, N. A. Stretchable nanoparticle conductors with self-organized conductive pathways. Nature, 500, 59-63 (2013).

65. Ma, R.;Kang, B.;Cho, S.;Choi, M.; Baik, S. Extraordinarily high conductivity of stretchable fibers of polyurethane and silver nanoflowers. ACS Nano, 9, 10876-10886 (2015).

66. Boland, C. S.;Khan, U.;Ryan, G.;Barwich, S.;Charifou, R.;Harvey, A.;Backes, C.;Li, Z.;Ferreira, M. S.; Möbius, M. E. Sensitive electromechanical sensors using

viscoelastic graphene-polymer nanocomposites. Science, 354, 1257-1260 (2016).

67. Kang, Y.;Wang, G.;Zhao, S.;Li, J.;Di, L.;Feng, Y.;Yin, J.; Zhu, J. High Resolution Printable and Elastomeric Conductors from Strain‐Adaptive Assemblies of Metallic Nanoparticles with Low Aspect Ratios. Small, 16, 2004793 (2020).

68. Koerner, H.;Liu, W.;Alexander, M.;Mirau, P.;Dowty, H.; Vaia, R. A. Deformation-morphology correlations in electrically conductive carbon nanotube—thermoplastic polyurethane nanocomposites. Polymer, 46, 4405-4420 (2005).

69. Sun, H.;Han, Z.; Willenbacher, N. Ultrastretchable conductive elastomers with a low percolation threshold for printed soft electronics. ACS applied materials & interfaces, 11, 38092-38102 (2019).

70. Larmagnac, A.;Eggenberger, S.;Janossy, H.; Vörös, J. Stretchable electronics based on Ag-PDMS composites. Scientific reports, 4, 1-7 (2014).

71. Liu, H.;Li, Y.;Dai, K.;Zheng, G.;Liu, C.;Shen, C.;Yan, X.;Guo, J.; Guo, Z. Electrically conductive thermoplastic elastomer nanocomposites at ultralow graphene loading levels for strain sensor applications. Journal of Materials Chemistry C, 4, 157-166 (2016).

72. Hu, Y.;Zhao, T.;Zhu, P.;Zhang, Y.;Liang, X.;Sun, R.; Wong, C.-P. A low-cost, printable, and stretchable strain sensor based on highly conductive elastic composites with tunable sensitivity for human motion monitoring. Nano Research, 11, 1938-1955 (2018).

73. Zhang, L.;Chen, K.;Wang, S.;Chen, S.;Niu, S.;Wang, Z.; Du, P. Synthesis of

percolative hyperelastic conducting composite and demonstrations of application in wearable strain sensors. Mater. Lett., 233, 306-309 (2018).

74. Wang, Y.;Zhu, L.;Mei, D.; Zhu, W. A highly flexible tactile sensor with an interlocked truncated sawtooth structure based on stretchable graphene/silver/silicone rubber composites. Journal of Materials Chemistry C, 7, 8669-8679 (2019).

75. Chen, L.;Lu, L.;Wu, D.; Chen, G. Silicone rubber/graphite nanosheet electrically conducting nanocomposite with a low percolation threshold. Polym. Compos., 28, 493-498 (2007).

76. Ding, H.;Zhong, M.;Wu, H.;Park, S.;Mohin, J. W.;Klosterman, L.;Yang, Z.;Yang, H.;Matyjaszewski, K.; Bettinger, C. J. Elastomeric conducting polyaniline formed through topological control of molecular templates. ACS nano, 10, 5991-5998 (2016).

77. Stoyanov, H.;Kollosche, M.;Risse, S.;Waché, R.; Kofod, G. Soft conductive elastomer materials for stretchable electronics and voltage controlled artificial muscles. Adv. Mater., 25, 578-583 (2013).

78. Sureshkumar, M.;Na, H. Y.;Ahn, K. H.; Lee, S. J. Conductive nanocomposites based on polystyrene microspheres and silver nanowires by latex blending. ACS applied materials & interfaces, 7, 756-764 (2015).

79. Lee, P. et al. Highly stretchable and highly conductive metal electrode by very long metal nanowire percolation network. Adv. Mater. 24, 3326–3332 (2012).

80. Chun, K.-Y. et al. Highly conductive, printable and stretchable composite films of carbon nanotubes and silver. Nature Nanotechnol. 5, 853–857 (2010).

81. Liu, K. et al. Cross-stacked superaligned carbon nanotube films for transparent

and stretchable conductors. Adv. Funct. Mater. 21, 2721–2728 (2011).